

The GALAH survey: Chemical homogeneity of the Orion complex

Janez Kos,¹★ GALAH team,²

¹*Faculty of Mathematics and Physics, University of Ljubljana, Jadranska 19, 1000 Ljubljana, Slovenia*

²

Accepted XXX. Received YYY; in original form ZZZ

ABSTRACT

Due to its proximity the Orion star forming region is often used as a proxy to study processes related to star formation and observe young stars in the environment they were born in. Orion is getting additional attention within the Gaia DR2, as distance measurements are now good enough that a three dimensional structure of the complex can be explored. Here we test a hypothesis that due to non-trivial structure and dynamics, and age spread in the Orion complex, a chemical enrichment of youngest stars by early core-collapse supernovae can be observed. We obtained spectra of 794 stars of the Orion complex with the HERMES spectrograph at the Anglo Australian telescope as a part of the GALAH and GALAH-related surveys. We use spectra of ~ 300 stars to derive precise atmospheric parameters and chemical abundances of 25 elements for 15 stellar clusters in the Orion complex. We demonstrate that the Orion complex is chemically homogeneous and that there was no self-pollution of young clusters by core-collapse supernovae from older clusters. With a precision of 0.02 dex in relative alpha abundance and 0.06 dex in Oxygen abundance we would be able to detect pollution from a single supernova given a fortunate location of the SN and favourable conditions for the ISM mixing. We estimate that the supernova rate in the Orion complex was very low, possibly producing no supernova by the time the youngest stars of the observed population formed (from around 21 to 8 Myr ago).

Key words: astrochemistry – surveys – stars: abundances – stars: formation – stars: pre-main-sequence – open clusters and associations

1 INTRODUCTION

Orion complex at a distance of around 400 pc is the nearest and most studied star-forming region. It serves as a proxy for the study of large, highly structured star forming regions with visible hierarchy. While most of the studies of star formation are focused into the Orion nebula cluster (ONC) and Ori A and their ongoing star formation, there are remnants of recent star formation (starting 21 Myr ago [Kos et al. \(2019\)](#)) in regions to the north and west of the ONC, and possibly in front of it ([Alves & Bouy 2012](#); [Kounkel et al. 2017](#); [Fang et al. 2017](#)).

Due to its proximity the Orion complex is the only large star forming region in which extensive, high resolution spectroscopic studies can be performed; hundreds of stars can be observed in a reasonable time. This fact, together with an interesting structure of the Orion complex (hierarchy, sequential star formation, nontrivial kinematics, unexplained origin), makes it a prime case to study chemical evolution of star forming regions. It has been observed in the past, that there are chemical inhomogeneities between stars and regions of the complex. In a series of papers [Cunha & Lambert \(1992, 1994\)](#); [Cunha et al. \(1995, 1998\)](#) analysed abundances of Li,

C, N, O, Si, and Fe, in a broad range of stellar types (18 B stars and 9 F and G stars) with great care, taking non-LTE effects into the account. They discovered a trend of younger regions of the complex having higher abundances of O and Si, while the abundances of C, N, and Fe are constant ([Cunha & Lambert 1994](#)). This has been attributed to younger regions being polluted by core collapse supernovae material from older regions. Most massive core collapse supernovae dominantly produce Oxygen ([Nomoto et al. 2006](#)), so this is indeed the expected signature of self-pollution. Others, however, do not see any correlation between age and chemical abundances in the complex ([Simón-Díaz 2010](#)), or even observed the opposite trend, at least in $[Fe/H]$ ([Biazzo et al. 2011a,b](#)). Such inconsistency (although the differences in absolute abundances between studies are minuscule) might as well be a consequence of a small number statistics. Matter of fact, we now resolve more clusters in the Orion complex than the stars studied in those papers ([Chen et al. 2019](#); [Zari et al. 2019](#)). This exposes another problem; within each region of the Orion complex are clusters of different ages, so by observing only a small number of stars any analysis of age-abundances trends is ambiguous.

Open clusters are most commonly used to demonstrate chemical homogeneity and most show high level of homogeneity ([Bovy 2016](#); [Casamiquela et al. 2019](#)). However open clusters represent

★ E-mail: janez.kos@fmf.uni-lj.si

only a small fraction of clusters that survived past 100 Myr. Arguably, these represent the most massive clusters born in least perturbed environments. The chemical homogeneity of their parent structures – whole star forming regions is not obvious. Star forming regions can be made inhomogeneous by most massive core collapse supernovae during the gravitational collapse of the cloud or could be intrinsically inhomogeneous due to their size and lack of time for the turbulence to homogenise the ISM. The Orion complex is perfect for such an inquiry, as it includes the λ Ori association, which does not appear to have had a direct contact with the rest of the complex in its lifetime. There is also a relatively large age spread observed in the complex which makes the possibility of self pollution by core collapse supernovae real.

With modern multi-object spectrographs it is possible to observe hundreds of stars with each pointing, effectively making a complete survey of Orion complex members within limiting magnitudes of such instruments. We use the 400 fibre HERMES instrument at the 3.9 m Anglo-Australian telescope at the Siding Spring observatory. Some data was taken by the GALAH survey and most by a dedicated survey performed by the GALAH team members. A similar survey was also done as part of the APOGEE 2 survey (Cottle et al. 2018; Kounkel et al. 2018). While such surveys cannot achieve the quality of dedicated star-by-star observations, the sheer quantity of data and contemporary analysis techniques can give more reliable picture of the chemical state of the complex.

In this paper we work on a hypothesis that the self pollution in the Orion complex is possible. This is supported by: (i) a relatively large spread of ages of stars (21 Myr to 6.5 Myr in observed regions), (ii) consistent ages within clusters, which also prove triggered, sequential star formation, (iii) non-trivial dynamics of the Orion complex, which puts older clusters into the vicinity of younger clusters at the time of their birth, and (iv) prior observations of chemical inhomogeneity, although observed in a small sample of stars. It must be noted that we did not observe the youngest regions in the complex (ONC and σ Ori region), so our findings are based on regions Ori OB1a, OB1b, λ Ori association and stars around NGC 1788. We study the chemical state and history of the Orion complex. Finding a complete history of star formation in the complex is not the scope of this paper, as we lack observations of youngest stars and stars less massive than $0.35 M_{\odot}$. We also trade completeness of our target selection for a more cautious target selection, most suitable for measuring abundances of chemical elements and having high membership probabilities for identified clusters. Dynamics of the complex is not addressed, mostly for the same reasons, but is admittedly of equal importance as ages and chemical composition in figuring out the relations between clusters.

Proving any self-pollution would be the only case where the population of stars responsible for the pollution is observed alongside the polluted population. On the other hand, observational proof that large, complex, structured star forming regions with measurable intra-region age spread are chemically homogeneous has important implications as well. This is a proposition on which some techniques in the galactic archaeology rely on. Chemical tagging is a method where stars from long ago dispersed structures can be related based on similar chemical abundances. This is inevitably a destiny of the Orion star forming region as well. While some more massive open clusters can survive a few billion years, most (> 90%) stars are dispersed much quicker. Eventually they lose all kinematic similarity to their star forming region and can only be matched to it by their unique chemical signature. Two questions must be answered before chemical tagging of disk stars is deemed feasible; Do stars from same star forming regions really have identical chemical

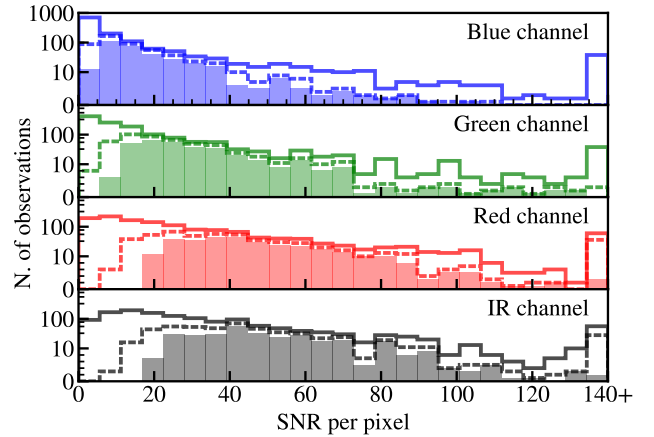


Figure 1. SNR distribution of all observed stars (solid lines), spectra where the parameter pipeline converged (dashed lines) and spectra used in the final analysis (filled histograms). Differences between the solid and dashed lines are due to hot stars (with not enough features for the pipeline to converge), binaries, fast rotators and other peculiar spectra. There are fewer stars in the final sample, as we rejected low SNR spectra (with $SNR < 20$ in the red arm), results with large uncertainties and moderately fast rotators ($v \sin i > 40 \text{ km s}^{-1}$). SNR per pixel is shown. SNR per resolving element is about twice as large.

signatures? And are we able to measure chemical abundances with good enough precision that 10 000s of different star forming regions can be discerned from each other?

Our data is described in Section 2. One should also read Kos et al. (2017); Buder et al. (2018), and Buder et al. (2020, in preparation) for a complete overview of the GALAH survey and the data reduction. Clustering algorithm, isochrone fitting, and photometric parameters and age determination are outlined in Section 3. Some more details are found in our previous paper on the ages of the Ori OB1a association (Kos et al. 2019). The bulk of our procedures are described in Section 4, where atmospheric parameters and abundances are calculated. We performed an unconventional, semi-Bayesian fit of synthetic stellar templates to observed spectra. Photometric quantities are propagated into spectral fitting and results are probability distributions for all calculated parameters. Use of such a pedantic approach is obvious when statistical evaluation of the chemical homogeneity is made in Section 4.3. Finally, we estimate the number of core collapse supernovae in the observed population in Section 5 and show that the observed IMF and good chemical homogeneity agree that there were most likely no supernovae that could have polluted the youngest populations in the Orion complex. Implications of this measurement are discussed in Section 6.

2 DATA

This work relies on the observing and data reduction infrastructure of the GALAH survey. Some data was taken as part of the regular GALAH survey, but most was obtained on a separate observing proposal in order to target darker stars. A list of targets was compiled based on *Gaia* DR2 alone. The Orion complex members were identified by clustering in the position-proper motion-parallax space. The same algorithm as explained in Section 3 was used. Radial velocities were ignored at this stage and the clustering was repeated with radial velocities taken into the account once the observations

were completed and all the data was reduced. This initial clustering was only used to make the observing strategy as efficient as possible. Fields from the regular GALAH survey were observed between 2014 and 2018 and the darker fields of the dedicated survey were observed in February 2019.

GALAH has a simple selection function and only observes stars between magnitudes $12.0 < V_{JK} < 14.0$, where the V_{JK} magnitude is a V magnitude calculated from 2MASS JHK photometry. A separate selection function is used for brighter targets observed during the twilight which have magnitudes $9.0 < V_{JK} < 12.0$. Unfortunately these selection functions prevent us to observe any but the brightest A and B dwarfs in the Orion complex. While some F stars fit into the observed magnitude range, they are less likely to be Orion complex members, because observed stars are picked at random from all stars in the correct magnitude range. GALAH selection function does not prioritise Orion members, so only a few Orion members were actually observed. To determine abundances of a large number of elements, F, G and K type stars are more suitable than A and B stars. Hence a special survey on a separate proposal was made to observe fainter targets. Instead of using a straightforward selection function, like one of GALAH, we first found Orion complex members using *Gaia* DR2 position-proper motion-parallax space and the same clustering algorithm as presented in Section 3. Radial velocities were ignored at this stage and the clustering was repeated with radial velocities taken into the account once the observations were completed and all the data was reduced. This initial clustering was only used to make the observing strategy as efficient as possible. Then the priority was given to stars with *Gaia* G magnitudes between 12.0 and 14.5 (roughly $12.25 < V_{JK} < 14.75$). Remaining fibres were filled with Orion members up to one magnitude darker. Orion complex members filled most of 2dF’s 400 fibres and any remaining fibres were positioned to capture field stars in the same magnitude range. Ori OB1a, OB1b, λ Ori and NGC 1788 regions were covered in the dedicated proposal. Exposure time for the fields in the separate proposal was extended by 60% compared to GALAH fields to accommodate for darker targets. Apart from the selection function, the quality of spectra is therefore comparable in both surveys.

Collectively in the GALAH survey and the dedicated proposal we observed 16 fields; 11 on a separate proposal, 4 regular GALAH fields and one bright GALAH field. The bright GALAH field only includes one Orion complex member and one regular GALAH field only includes 3. All together we observed 794 members. Most of the observed stars were not analysed fully. Final analysis of chemical homogeneity omits many stars as they are too dark for anything more than a radial velocity measurement (48% of all observed stars). These stars still help constrain the isochrone fits used for age measurements. Stars are also absent from the final analysis, if they are too hot (6%), are fast rotators (4%), or are double lined binary stars (1%). Some spectra were rejected based on poor fits of spectral templates (6%). This statistics is illustrated in Figure 1. Almost 20% of stars were observed repeatedly over an interval of years (due to the overlap between the GALAH program and the dedicated Orion observing program) or days (due to poor weather conditions during the dedicated Orion observing program).

All fields/spectra were reduced with the same GALAH pipeline, regardless from which survey they were taken. Spectra from the dedicated survey can therefore be used within the GALAH ecosystem. Our analysis pipeline, however, is unique and is described in the following two sections.

3 CLUSTERING AND AGES

3.1 Clustering

Our goal is to measure precise relative chemical abundances, which is much easier to do, if measurements of individual stars can be combined to increase precision. Obviously, the measurements over a natural group of stars must be combined. The next largest structure after individual stars in the hierarchy of the complex are clusters. These do not necessarily have to be open clusters, but any reasonably large overdensities we can detect. We consider such clusters the basic building blocks of the complex; stars in each clusters are assumed to be born at the same time, in a small region. Therefore these clusters are most likely – and indeed assumed to be chemically homogeneous. Chemical abundances measured as an average over the clusters can then be measured more precisely than the abundances of individual stars.

Clusters in the Orion complex are rarely well isolated from their environment. Clustering the complex is a challenging task and is extensively explored in the literature, particularly succeeding the *Gaia* DR2 (Kounkel et al. 2018; Zari et al. 2019; Chen et al. 2019; Kos et al. 2019). In general the identified clusters match between different authors.

We employed a similar approach to clustering the Orion complex as in Kos et al. (2019), so we only give a brief review of the method here. Clusters were found by ENLINK (Sharma & Johnston 2009) separately for the Ori OB1 region and the λ Ori region. The former also included the ONC and σ Ori cluster. In the Ori OB1 region we fixed the number of clusters to 16, as such clustering seemed plausible given the ENLINK hierarchy. 11 of them lie in the region of our interest (see green polygons in Figure 2). Other 5 had to be considered as well, otherwise stars belonging to the σ Ori cluster, for example, but lying close to the Ori OB1b clusters could be mis-clustered (note black points inside green polygons in Figure 2). In λ Ori association the ENLINK clustering was more ambiguous. A small variation in parameters returned between two and 6 clusters. While two clusters are more likely, we divided the region into four clusters to check for possible chemical variations in stars close to the centre of the association as opposed to two “tails” stretching to the north-west and south-east.

From the ENLINK clustering we only used the centres of clusters and then found cluster members following the same approach as in Kos et al. (2019): we defined a metric

$$d = \frac{\arccos(\mathbf{r} \cdot \bar{\mathbf{r}})}{1.25^\circ} + \frac{\sqrt{(\mu_\alpha - \bar{\mu}_\alpha)^2 + (\mu_\delta - \bar{\mu}_\delta)^2}}{1.0 \text{ mas yr}^{-1}} + \frac{|\varpi - \bar{\varpi}|}{0.22 \text{ mas}} + \frac{|v_r - \bar{v}_r|}{15.0 \text{ km s}^{-1}}, \quad (1)$$

where bars denote positions, proper motions, parallax and the radial velocity of a cluster centre. First term describes the distance on the sky. Stars with normalised distance $d < 4.0$ from a cluster centre are made members of that clusters. If more than one cluster centre is within this distance, a star is made a member of only the nearest one. If no cluster centre is within $d < 4.0$ of a star it is designated a field star. Wherever no radial velocity is available, we only use the first three terms in Equation 1 and scale the distance accordingly. This is described in more details in Kos et al. (2019).

After each star is assigned a cluster (or is left as a field star) we recalculate cluster centres and repeat the above process until it converges (so more than 98% of stars do not change cluster memberships after the final iteration, around 5 iterations are needed). Final cluster members are illustrated in Figure 2. Individual clusters

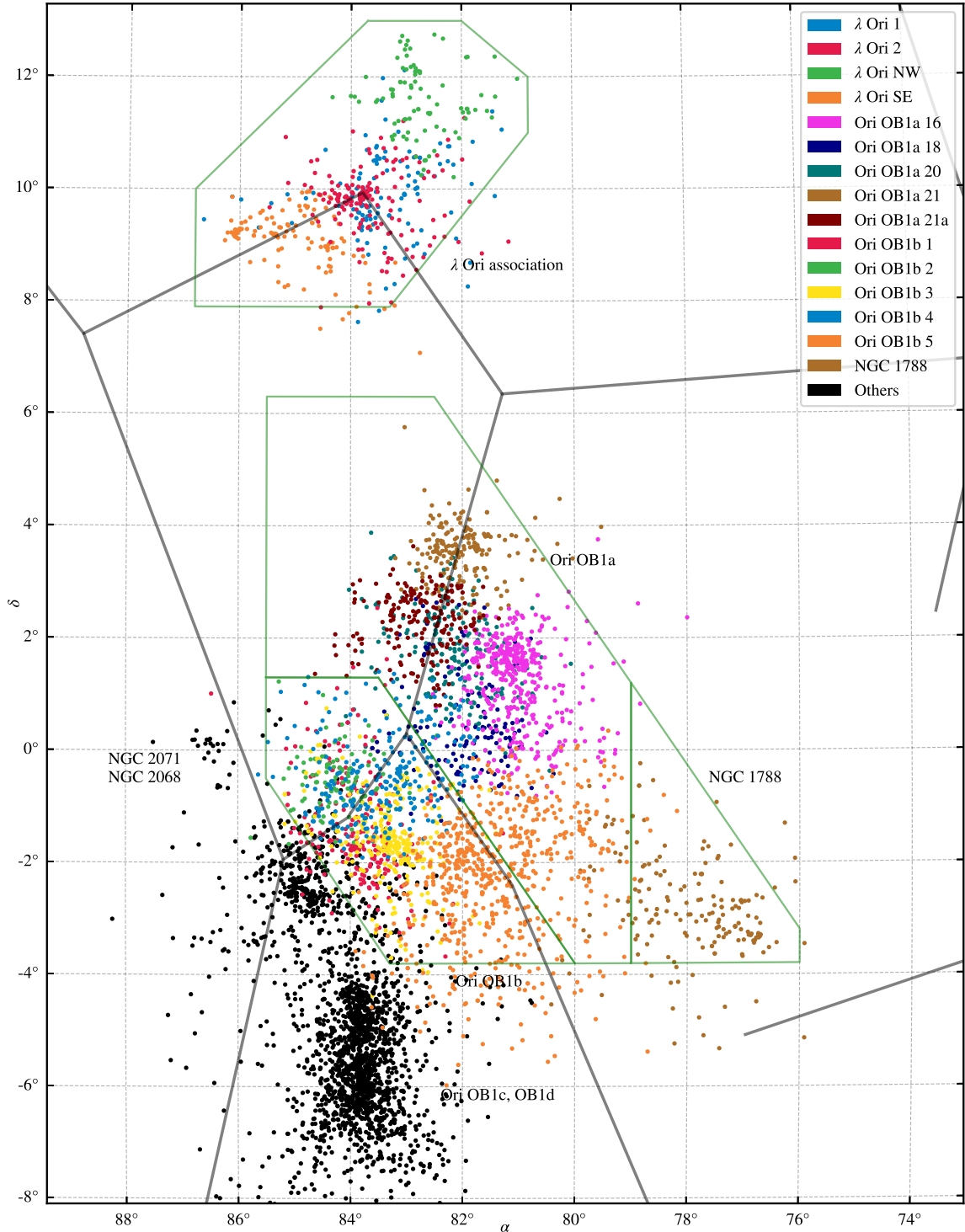


Figure 2. Orion complex with stars belonging to our clusters marked in colour. Green polygons show the region analysed in this work. 15 clusters in these regions are marked in colour. Black stars belong to other constituents of the Orion complex and are not analysed in this work.

in a 6D space are shown in Appendix B and a list of members is available at CDS. Centres defining the cluster are collected in Table 1.

3.2 Isochrones fitting and ages

We use *Gaia* photometry to derive T_{eff} and $\log g$ of each star and calculate ages (see Table 1) of clusters. We produced Padova isochrones (Bressan et al. 2012; Chen et al. 2014; Tang et al. 2014) for the *Gaia* magnitudes using the photometric system by Maíz Apellániz

Cluster	α °	δ °	$\mu_\alpha \cos \delta$ mas yr ⁻¹	μ_δ mas yr ⁻¹	ϖ mas	v_r km s ⁻¹	age Myr
λ Ori 1	83.545	9.865	1.643	-2.165	2.42	29.7	9.2±1.8
λ Ori 2	83.775	9.844	0.787	-2.097	2.45	27.6	6.5±1.3
λ Ori NW	82.810	11.347	1.343	-1.666	2.49	24.9	6.5±1.3
λ Ori SE	84.577	9.081	1.440	-2.500	2.50	27.8	7.0±1.4
Ori OB1a 16	81.057	1.304	1.326	-0.169	2.85	21.2	11.7±1.2
Ori OB1a 18	81.929	0.317	0.241	1.174	2.37	28.3	12.7±1.3
Ori OB1a 20	82.140	1.637	-0.598	0.687	2.69	29.7	21.2±2.1
Ori OB1a 21	82.052	3.561	1.432	-0.561	2.86	20.0	11.0±1.1
Ori OB1a 21a	82.786	2.344	1.685	-0.412	2.81	20.6	12.5±1.2
NGC 1788	77.820	-2.896	1.249	-0.724	2.64	22.8	8.5±2.1
Ori OB1b 1	83.824	-1.594	-1.267	1.048	2.33	28.8	17.0±3.4
Ori OB1b 2	84.226	-0.474	-1.014	-0.705	2.51	32.6	16.5±3.3
Ori OB1b 3	83.192	-1.711	0.051	-0.230	2.36	30.5	13.0±2.6
Ori OB1b 4	83.268	-0.522	1.666	-1.004	2.78	21.6	9.0±1.8
Ori OB1b 5	81.596	-2.029	1.148	-0.910	2.82	22.5	11.5±2.3

Table 1. Parameters defining cluster centres (columns 2–7) as used in our membership determination algorithm. We also added a column showing measured ages (not used in the membership determination algorithm).

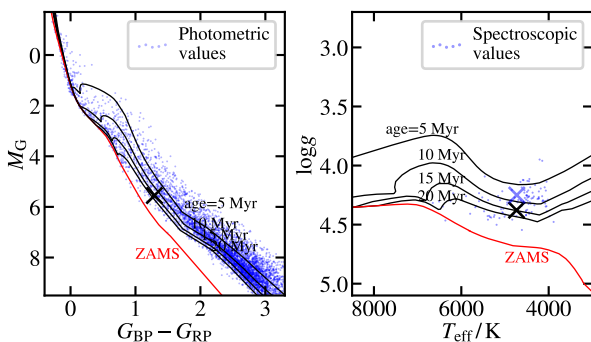


Figure 3. Left: HR diagram of all our members of the Orion complex. Right: A Kiel diagram of stars with spectroscopic T_{eff} and $\log g$. Zero-age-main-sequence (ZAMS) and isochrones for ages of 5, 10, 15, and 20 Myr are plotted with other parameters being representative of the Orion complex. One star is marked with \times in both panels to illustrate the discrepancy of spectroscopic $\log g$. In the right panel the black \times indicates T_{eff} and $\log g$ calculated photometrically and the blue \times indicates T_{eff} and $\log g$ measured from spectra alone. The difference in $\log g$ is 0.13 dex – equivalent to ~ 7 Myr (or 50%) difference in age.

& Weiler (2018). Age and interstellar extinction were the only free parameters. Metallicity was assumed to be $[M/H] = -0.05$. We found the best fitting isochrone by eye, same as in Kos et al. (2019). Differential reddening is low in Ori OB1a region (see Kos et al. 2019), but significant everywhere else. Due to the lack of proper data to precisely measure reddening of individual stars, we determined mean reddening by isochrone fitting and increased the age uncertainty for clusters in the remaining regions. One can see in Appendix C that the structures of MS and PMS are well visible in HR diagrams for all clusters. Hence we conclude that the differential reddening has a limited effect on measured ages. Once the isochrone is determined, the nearest point on the isochrone to each star gives its mass, T_{eff} , $\log g$ etc. Even more, given the uncertainties of *Gaia* magnitudes, the probability density functions for each parameter can be acquired. Age is used later in this paper to estimate the number of supernova explosions in the observed population (Section 5). Temperature and gravity are needed to correctly marginalise measured stellar parameters over T_{eff} and $\log g$.

$\log g$ is measured from the HR diagram much more accurately

than one could from the spectra. Precision of $\log g$ in GALAH spectra is extensively discussed in (Buder et al. 2018) and is, depending on the method used, worse than 0.1 dex. Temperature can be measured much more precisely in this regard. Therefore a small variation in temperature does not change the gravity measurement much (although both correlate, as seen in Figure 5). Age dependence is the exact opposite, so measuring ages well is critical for gravity estimation from the HR diagram (illustrated in Figure 3). Given our age estimates and typical photometric uncertainties, a typical photometric $\log g$ uncertainty is 0.05 dex and a typical photometric temperature uncertainty is 60 K.

4 SPECTROSCOPIC PARAMETERS AND ABUNDANCES

4.1 Bayesian fitting schema

The following subsection gives a general description of our approach to fitting parameters and abundances. Some steps are then described in more details in Sections 4.1.2 to 4.1.5.

4.1.1 General description

To fit spectroscopic parameters and abundances we wanted to include the photometric information (T_{eff} and $\log g$) into the fitting schema. In the most basic implementation, one could leave photometric T_{eff} and $\log g$ fixed when fitting other spectroscopic parameters, but this approach has a few dangerous drawbacks. Photometric and spectroscopic parameters do not necessarily represent the same quantities in practice; photometric and spectroscopic T_{eff} , for example, might not measure the same temperature. Even if the definition of T_{eff} is defined consistently, line lists and models of stellar atmospheres can be different among photometric systems. This can lead to large systematic errors for spectroscopic parameters. But more importantly, aiming for most precise chemical abundances possible, one should marginalise the calculated abundances over other measured parameters. This means that a single value for T_{eff} and $\log g$ is not sufficient, but a PDF must be used in all calculations.

The above reasons led us to adopt a Bayesian fitting schema, where we can propagate photometrically measured T_{eff} and $\log g$ throughout the spectral fitting procedure. To fit the spectra we employ SME (Valenti & Piskunov 1996; Piskunov & Valenti 2017)

software via iSpec wrapper (Blanco-Cuaresma et al. 2014; Blanco-Cuaresma 2019) to produce synthetic spectra. These are fitted to normalised observed spectra.

Two different fits are made. First we fit the whole spectrum in all four bands to obtain the overall metallicity ($[M/H]$), alpha abundance ($[\alpha/Fe]$), projected rotational speed ($v \sin i$), and spectroscopic T_{eff} and $\log g$. $v \sin i$ is the only fitted broadening parameter. v_{mic} and v_{mac} are used in the calculation of the synthetic spectra, but are estimated by iSpec from empirical relations (Jofré et al. 2014). Because observed stars are young, most are rotating fast enough that rotational broadening dominates over turbulence broadening. Elemental abundances are fitted separately where each element is fitted independently from others.

In both cases, to fit atmospheric parameters and abundances, the log-likelihood is written as

$$\ln P(f|\lambda, \sigma_f, \Theta) = -\frac{1}{2} \sum_n \frac{(f_n(\lambda) - s_n(\lambda|\Theta))^2}{\sigma(\lambda)_f^2}, \quad (2)$$

where f and s represent the observed and synthetic spectra, the former having the uncertainty σ_f . Θ are parameters of the synthetic spectrum (temperature, gravity, metallicity, etc.), and λ is the wavelength. Posterior probability for the fitted parameters is

$$P(\Theta|f, \lambda, \sigma_f) \propto P(\Theta)P(f|\lambda, \sigma_f, \Theta). \quad (3)$$

Prior $P(\Theta)$ includes all the photometric information.

When fitting the whole spectrum the prior for T_{eff} is the PDF of the photometric temperature with the mean value corrected (see discussion on differences between photometric and spectroscopic temperature in Section 4.1.4). Prior for $\log g$ is just the PDF of the photometric gravity. We assume geometric distances from Bailer-Jones et al. (2018). Due to the proximity of the Orion complex, there is no need to improve distances by taking cluster membership into the account. For the remaining parameters ($[M/H]$, $[\alpha/Fe]$, and $v \sin i$) we use flat priors within some bounds.

When fitting spectral lines of individual elements, the priors for T_{eff} , $\log g$, $[M/H]$, $[\alpha/Fe]$, and $v \sin i$ are PDFs of the initial fit. The PDF is represented by a multivariate Gaussian. This is a simplification, but from our experience the aforementioned PDF is indeed similar to a Gaussian and there is no visible improvement when a more complicated representation of the PDF is used.

The posterior distribution is calculated by the `EMCEE` code (Foreman-Mackey et al. 2013). It turns out that calculating a synthetic spectrum at every step of MCMC is too time consuming. Instead we produce a grid of synthetic templates and interpolate a template in each step of MCMC from that grid. This is much faster only if the number of spectra in a grid can be much smaller than the number of required MCMC steps. Otherwise a synthetic template spectrum should be calculated with every step of MCMC. In general, for a problem like ours, one needs ~ 50 walkers. Based on our experimentation, around 50 steps are needed for the chains to stabilise (in the so called burn-in phase) and tens more to sample the distribution. On top of that only $\sim 20\%$ of the steps are actually accepted. These are minimum requirements to produce useful results with well-behaved spectra. So in practice one would have to calculate in the order of 10 000 synthetic templates to fit one spectrum with MCMC. One can achieve a significant improvement, if a representative grid can be made from fewer synthetic spectra (see Section 4.1.4).

The results of the fitting process are PDFs for all fitted parameters and abundances. We use PDFs in the rest of our analysis whenever possible. Sometimes mean values are used, especially to make some illustrations comprehensible.

4.1.2 Resolution equalisation

Observed spectra have a nominal resolving power of 28 000. Real resolving power varies with wavelength, from fibre to fibre and with time as well. Variation in wavelength is the strongest, with the resolving power dropping to around 23 000 in some corners of the detector. It is followed by fibre-to-fibre variations, as not all fibres produce the same sized beam and are not positioned in the pseudo slit precisely enough. The latter causes some fibre bundles to be slightly out of focus in respect to other bundles. Variations in time occur, if the focus of the spectrograph changes throughout the night.

To account for a varying resolution, the synthetic spectra must have the same resolution profile as the observed spectra. Synthetic spectra that can be produced at a very high resolution could be degraded to whatever is the resolution profile of the observed spectrum. This approach introduces some complications. Each observed spectrum has a different resolution profile, which requires one more operation each time a synthetic spectrum is calculated. More important is that the resolution profile is not well known. Therefore the observed spectrum and a resolution-corrected synthetic spectrum might still have relatively very different resolution profiles.

Instead we degraded all observed spectra so they have a constant resolution profile with $R = 22\,000$. By degrading the resolution of observed spectra, the precise knowledge of the initial resolution profile become less important. For a resolution degradation from $R = 28\,000$ to $R = 22\,000$, an uncertainty of 10% in initial resolving power is reduced to an uncertainty of 3.9% in the final lower resolution spectrum. 10% uncertainty is indeed plausible for our spectra. Only synthetic spectra with a constant resolving power of $R = 22\,000$ are needed after such an operation.

4.1.3 Spectrum normalisation

Even-though the reduction pipeline provides normalised spectra, the normalisation is too crude to be used in the process described here. For this purpose we produce a synthetic spectrum with photometric T_{eff} and $\log g$, $[M/H] = -0.07$, $[\alpha/Fe] = 0$ and $v \sin i$ estimated with iSpec. Observed and synthesised spectrum are divided and the result is fitted by a high order polynomial (between orders 9 and 15, depending on the spectral band and the temperature of the star) representing the continuum. Because the spectra are expected to have similar $[M/H]$, $[\alpha/Fe]$, such method is reliable and robust and we do not change the continuum at any point during the following process, not even calculating a local continuum when fitting individual lines.

4.1.4 Initial conditions

While the MCMC algorithm itself does not need precise initial conditions, it pays off to estimate all the parameters as well as possible before fitting them. The main reason is that we produce a new grid for every star and want it to be as small as possible, as long as it can contain the space sampled by MCMC. Initial conditions thus define the centre of each grid.

Initial condition for $v \sin i$ is calculated from the spectra themselves by template fitting. Even without a well known T_{eff} and metallicity one can get the $v \sin i$ known to within a couple of km s^{-1} . It is calculated in a similar way to other parameters later: a grid of synthetic spectra is calculated with different $v \sin i$ assuming the photometric temperature, $[M/H] = -0.05$ and $[\alpha/Fe] = 0.0$. Grid is interpolated and the best matching $v \sin i$ is found.

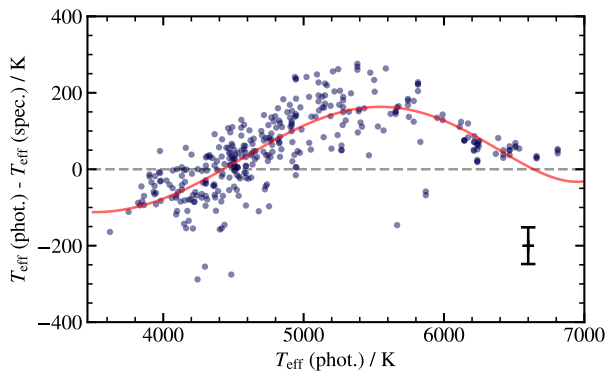


Figure 4. Difference between photometric and spectroscopic temperatures. Red line shows the relation used to construct the initial condition for the spectroscopic temperature from its photometric counterpart.

Initial condition for the temperature is a slightly modified photometric temperature. We found the photometric and spectroscopic temperatures match in first order. However, there is a deviation of ~ 160 K in the 4700 to 6200 K range (see Figure 4). It is consistent enough that we can guess how different the photometric and spectroscopic temperatures will be to adjust the initial condition accordingly. Such fine tuning is not done to get a better temperature measurement or faster convergence, but to be able to make the grid as small as possible. Improvement of the initial condition for 160 K means the grid can be two or three nodes smaller in the temperature dimension, which results in a significant improvement of the computing time.

Because Orion complex seemed to be very chemically homogeneous at first inspection, the initial conditions for metallicity and α abundance are $[M/H] = -0.05$ and $[\alpha/Fe] = 0.0$. Initial conditions for these two parameters are not that relevant, as the grid has to be relatively more extensive for them. A too small grid acts as a determinational prior, which we want to avoid, as metallicity and α abundance are the parameters we want to find.

4.1.5 Grid

As justified in Section 4.1.1, it is more feasible to interpolate synthetic spectra from a small grid than producing them at every step of the MCMC algorithm. Here we explore how dense the grid must be to not introduce systematic errors into the synthetic spectra.

To evaluate how dense must the grid be, we produced Figures A1 – A4. These figures show the maximum error of grid-interpolated synthetic spectra compared to synthetic spectra calculated directly by SME for the same set of parameters. Only the figures for the step sizes actually used by our analysis are shown ($\Delta T_{\text{eff}} = 70$ K, $\Delta[M/H] = 0.05$ dex, $\Delta[\alpha/Fe] = 0.05$ dex, and $\Delta(v \sin i) = 2.5$ km s $^{-1}$).

Some spectral lines seem to be very susceptible to non-linear effects and cannot be interpolated well, even with higher order splines (cubic splines were used in this work). Surprisingly the non-linear effects are limited to narrow temperature or metallicity range. We conclude that such phenomena are a product of SME or iSpec. These errors can be reduced by a finer grid, but not eliminated. However, a much finer grid is not feasible for our application. Such errors do not exist in the $v \sin i$ plot (Figure A4), as rotational broadening is accounted for by iSpec independently from the SME spectral synthesis code. Errors of interpolated spectra can be neglected, if they are much smaller than the uncertainty of observed

Parameter	Atmospheric parameters		Elemental abundances	
	# of nodes	step size	# of nodes	step size
T_{eff}	7	70 K	3	70 K
$\log g^1$	3	0.12 dex	3	0.1 dex
$v \sin i$	3	2.5 km s $^{-1}$	/	/
$[M/H]$	9	0.075 dex	/	/
$[\alpha/Fe]$	9	0.075 dex	/	/
$[X/Fe]$	/	/	30	0.1 dex
Total # of nodes	1701		270	

¹ $\log g$ dimension of the grid is omitted in practice, as marginalisation over $\log g$ had no impact on our derived PDFs (see text for explanation).

Table 2. Grid sizes. Atmospheric parameters and elemental abundances are fitted separately, hence two grids are needed. Parameters not used in one of the grid are marked with “/”.

spectra (typical SNR per pixel is 40, but can be as high as 100). This is true in all the cases, except for aforementioned lines suffering from the strongest non-linear effects. However the number of such lines is small and the error is still smaller than the flux uncertainty (just not much smaller), so they have negligible influence on derived stellar parameters.

Similar as for grid density, the grid boundaries must be as tight as possible to reduce computational time. Figure 5 shows a typical PDF. If initial conditions (defining the centre of the grid) are chosen well enough, there is no need for the grid to be orders of magnitude larger than the uncertainties. Grid sizes are given in Table 2. Note that such small grids are not suitable to fit atmospheric parameters or abundances for strong outliers. They are, however, large enough to detect them. If the MCMC algorithm requires a synthetic spectrum with parameters outside the grid, a spectrum at the grid edge is returned. This effectively acts as a flat prior for all parameters.

In the process we discovered that our results are the same, if we do not marginalise the abundances PDFs over $\log g$ but instead assume photometric $\log g$ (as we always do for the initial condition). The reason is that $\log g$ can be calculated much more precisely from fitted isochrones than we ever could spectroscopically. The likelihood is pretty much independent of any $\log g$ variabilities within the photometric $\log g$ error bars, which means that having $\log g$ as a free parameter is irrelevant. Therefore we can use grids without $\log g$, which reduces computational time significantly.

With the grid sizes discussed above, and the number of spectra in our sample, we conclude that it is more feasible to produce a small grid for each star as opposed to one giant grid spanning the parameter space of all observed stars. The grid is interpolated by cubic splines. The chosen interpolation algorithm is Scipy’s `ndimage.map_coordinates` (Virtanen et al. 2019) for its fast performance in multiple dimensions and ability to choose higher order splines as interpolation functions.

4.2 Validation

Figure 5 analyses the differences between using photometric T_{eff} and $\log g$ priors in the fitting schema. Mean values for $[M/H]$ and $[\alpha/Fe]$ do not change much, but the uncertainty is significantly improved when priors are used. Lower uncertainty consequently has an effect on the level of measured chemical homogeneity as we compare actual PDFs and not just mean values of $[M/H]$ and

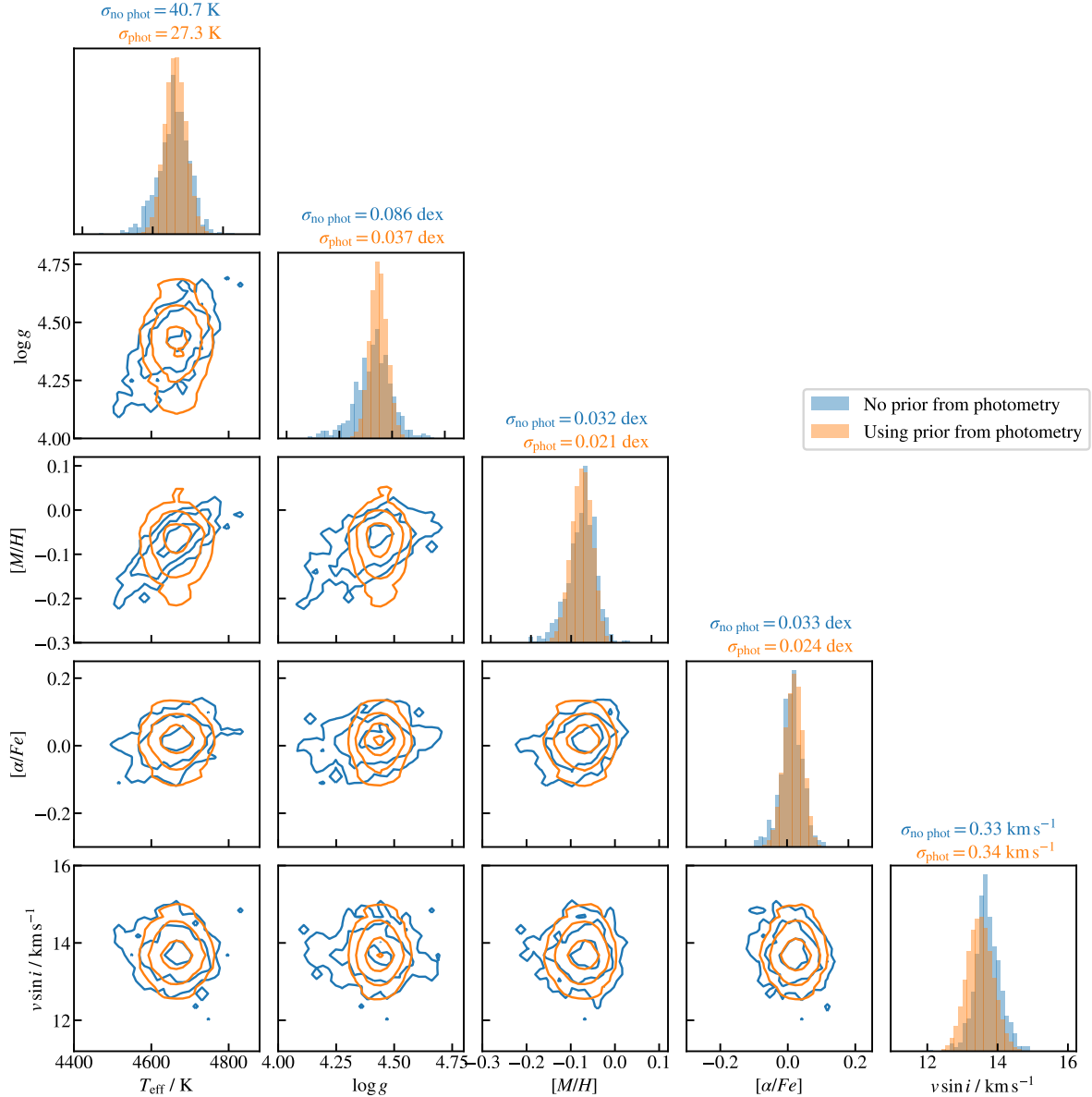


Figure 5. Corner plot showing the PDF of fitted parameters for one star without (blue) or with (orange) using priors on T_{eff} and $\log g$. Both priors are obtained from the isochrone fitting onto the HR diagram. Precisions of metallicity and alpha abundance that have otherwise non-determinant priors improve significantly when photometric priors are used. Some correlations also disappear.

$[\alpha/Fe]$. Uncertainty of $v \sin i$ does not improve, but the mean value does change.

In the fields observed in the special program we targeted members regardless of whether they were already observed in the GALAH survey. Due to poor weather we also observed some fields over several nights. Before combining observations over all epochs, we analysed individual spectra in order to estimate statistical and systematic uncertainties from repeated observations. Most observations were repeated with the same fibre (same fields observed over several nights), but some were also done with a completely different fibre configuration (overlaps between the GALAH survey and the special program). Analysis of repeated observations is shown in Figure 6.

Uncertainties calculated by a Bayesian schema are just statistical uncertainties – a consequence of noisy spectra, blended spectral

lines, etc. Systematic uncertainties arise mostly from stars being observed with different fibres which are affected by different optical aberrations. We tried to correct for that by reducing and equalising the resolution of observed spectra, but any errors in the resolution profile are still reflected in our parameters and abundances. Scatter of metallicity and alpha abundance in each cluster is larger than one would expect from statistical uncertainties alone. We attribute this to changing resolution across the CCDs, as the discrepancy between the statistical uncertainty and scatter of metallicity and alpha abundance becomes lower, if only spectra with more consistent resolution profile from the middle of the CCDs are used. This indicates that the resolution profile plays a crucial role, if very precise parameters and abundances are desired.

While the above is true for parameters measured across a wide range of wavelengths ($[M/H]$, $[\alpha/Fe]$), individual abundances suf-

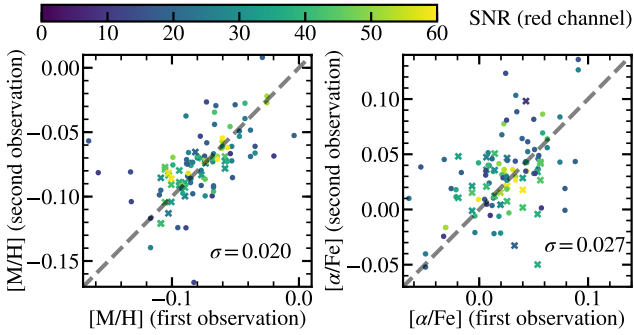


Figure 6. Analysis of repeated observations. Differences between repeats are shown for the measured metallicity (left) and alpha abundance (right). Circles show observations repeated with the same fibre and crosses show observations repeated with different fibres. Colour marks the lower of the two SNRs in the red channel. Only mean values of measured metallicities and alpha abundances are shown here. Scatter around the linear relation is given in each panel. It is larger than a typical measured uncertainty (see Figures 7 and 8), as mostly low SNR observations were repeated due to bad weather conditions.

fer even more from systematic errors. Wavelength ranges where abundances are measured were carefully selected and we did not modify them from what is used in GALAH’s DR2 (Buder et al. 2018). However a small perturbation in continuum or a nearby spectral line that might be characteristic for spectral types considered in this work can contribute some systematic uncertainty. Such contributions are very hard to analyse and we do not wish to do it here.

4.3 Detrending and relative abundances

Figures 9, 10, and 11 show measured metallicity, alpha abundance and abundances of 25 elements as a function of temperature. It is obvious that all parameters show trends that are the same (within our precision) for all clusters, regardless their age or location. The following contributes to the trends: (i) LTE approximation. We did no correction for non-LTE or 3D effects, because we detrend all parameters anyway. Assuming the non-LTE and 3D corrections are a smooth function of temperature, they are irrelevant after detrending. (ii) Systematic errors. These are particularly important for abundances of individual elements. While only a small region around a line of interest is used to fit a model spectrum to observations, the region is not always clear of other lines. This is sometimes hard to take into the account (by changing region boundaries, for example), especially if stars with a wide range of temperatures are being compared. (iii) Insufficient model spectra. Model spectra cannot incorporate all physical processes. This reflects in biases we observe as trends. Some trends might be even more pronounced, as we are dealing with PMS stars, which might not have model spectra calculated as carefully and rigorously as main sequence stars. Chromospheric activity (Carter 1989) and strong magnetic fields (Basri et al. 1992; Johns-Krull et al. 1999) are known to influence PMS stars significantly. (iv) Biased photometric temperature and gravity could have an effect as well, although it must be minor, as this is the only effect we thoroughly analysed.

Detrending removes any systematic trends and non-LTE trends well, but can not improve the accuracy of absolute abundances. For absolute abundances we have to know the physics responsible for the trend. More precise absolute abundances can only be obtained

by taking non-LTE effects into the account. In this work we neglect any non-LTE effects and resort to detrending. However, most of our stars are included in the GALAH DR3 (Buder et al., 2020, in preparation), where a lot of effort was put into non-LTE abundance determination. The drawback of GALAH DR3 is that the precision is lower than in this work, as stars are not assumed to be cluster members anywhere in the analysis process. Our work constrains relative chemical differences in the Orion complex much better than GALAH DR3 (see Table 3), but GALAH DR3 probably gives better mean absolute abundances. However, absolute abundances must not be taken for granted, as most stars are PMS stars, which again are not treated any different from MS stars in the GALAH DR3 pipeline.

For the purpose of relative chemical abundances we assume that none of the observed trends with T_{eff} and $\log g$ or $v \sin i$ are intrinsic. However, we are interested in trends with age or location, which could be a sign of chemical pollution. We do not observe trends of metallicity, alpha abundance or the abundance of any of the 25 elements against any of the remaining measured atmospheric parameters (T_{eff} and $\log g$, $v \sin i$) but temperature. Relative metallicity, alpha and elemental abundances are then calculated by removing the trend with temperature. A cubic spline is fitted as illustrated in figures 9, 10, and 11. Nodes were selected at an interval of 250 K, but some were removed, so there were at least 15 data-points between each node. Three steps of a symmetric sigma clipping algorithm with a threshold of 2.5σ were done for the final fit.

A simple chi-square test shows that the observed region of the Orion complex is chemically homogeneous in metallicity, alpha abundance, and all elements but Lithium whose homogeneity is not expected anyway. Li is gradually depleted early in the star’s life and the Li abundance evolution is not understood well enough to predict it at the level of homogeneity we observe here for other elements. Reduced χ^2 test calculated for 15 clusters and for element x is

$$\chi^2(x) = \frac{1}{14} \sum_{\text{clusters}} \frac{(\varepsilon_{\text{cluster}}(x) - \overline{\varepsilon}(x))^2}{\sigma_{\text{cluster}}(x)^2 + \sigma_{\text{int}}(x)^2}, \quad (4)$$

where $\varepsilon_{\text{cluster}}(x)$ is the mean abundances of element x in one cluster. $\sigma_{\text{cluster}}(x)$ equals the measured scatter divided by the square-root of number of stars in that cluster. $\sigma_{\text{int}}(x)$ is the intrinsic uncertainty of individual measurements. For most elements the reduced χ^2 value is around 0.4, except for Lithium where it is 2.9.

4.4 Absolute abundances

Detrending improves precision of our results, but contends the accuracy of absolute abundances reported in Table 3. Therefore we report (in Table 3) abundances after they are detrended and then being normalised to either the mean or the value at the Solar temperature (5770 K). One must be careful when comparing our absolute abundances to other measurements, especially for elements that show strong trends, like O, Y, Rb, Ce, and Zr.

5 ESTIMATING THE NUMBER OF SUPERNOVAE

To discuss the implications of a high chemical homogeneity all over the Orion complex, we want to estimate the number of SNe that exploded since the first stars in the complex were formed. One way is to integrate the IMF to calculate the expected number of massive stars that had time to explode as core-collapse SNe.

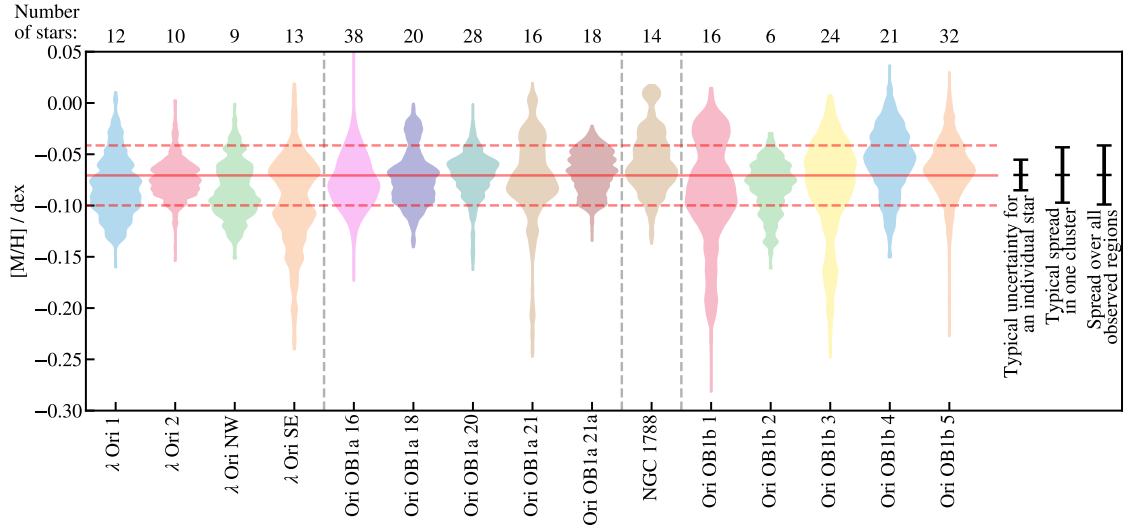


Figure 7. Probability distribution of metallicity for all observed clusters. Each violin plot is composed of all samples of the marginalised metallicity for each analysed star. Number of stars in each cluster is given on the top. Solid horizontal line shows the mean and dashed horizontal lines show the standard deviation of the whole sample. Typical scatter of samples for individual stars is shown on the right, together with a typical scatter in one cluster and the whole region. Vertical lines divide traditional regions of the Orion complex. Colour scheme for the clusters is the same as used in Section 3.

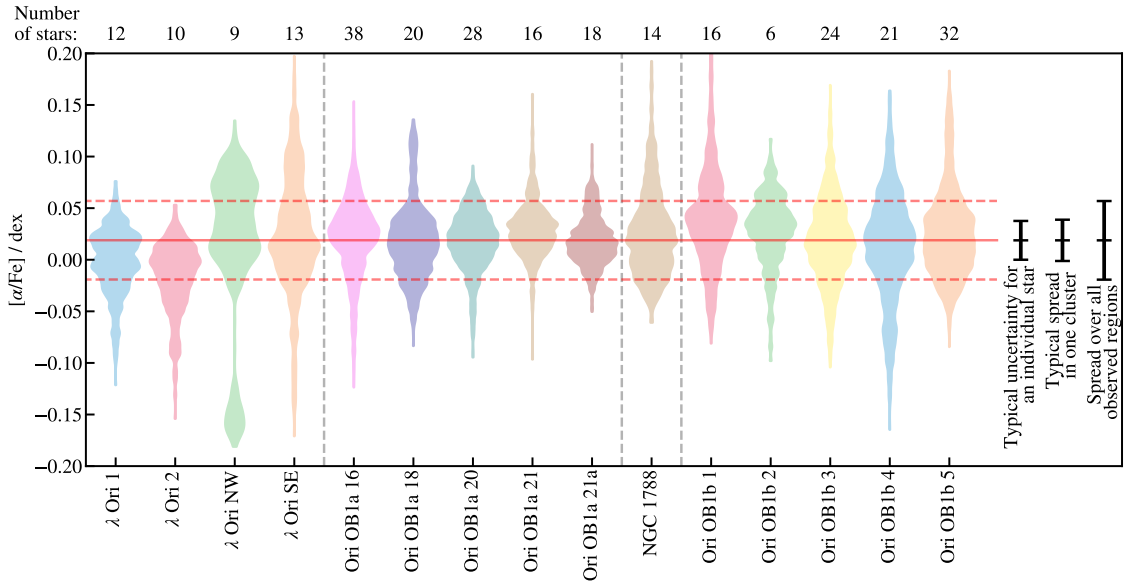


Figure 8. Probability distribution of alpha abundance for all observed clusters. Each violin plot is composed of all samples of the marginalised alpha abundance for each analysed star. Number of stars in each cluster is given on the top. Solid horizontal line shows the mean and dashed horizontal lines show the standard deviation of the whole sample. Typical scatter of samples for individual stars is shown on the right, together with a typical scatter in one cluster and the whole region. Vertical lines divide traditional regions of the Orion complex. Colour scheme for the clusters is the same as used in Section 3.

We estimated the masses of our members from the fitted isochrones. Because our selection is not complete and is in fact quite conservative, we also made a different selection with very relaxed criteria to be complete wherever the Gaia DR2 is. DR2 is complete between $12 < G < 17$ and almost complete between $7 < G < 17$. For the purpose of calculating the IMF, We selected stars in a parallax range $1.8 \text{ mas} < \varpi < 3.5 \text{ mas}$, proper motion $\mu = \sqrt{\mu_\alpha^2 + \mu_\delta^2} < 3.5 \text{ mas yr}^{-1}$, and at all magnitudes (but kept track of the completeness boundaries). Among those stars we selected all that are within $d < 8.0$ of any of the 15 clusters, where d

is defined in Equation 1. Allowing distant stars to be members of our clusters means many stars might not have their membership determined well, but the membership of the whole complex is more complete. We also cleared the sample of any stars that can be rejected based on their position on the HR diagram, same as we did in the initial membership determination. Thus observed mass distribution is shown in Figure 13. We fitted a Kroupa (Kroupa 2001) IMF to the region where our data is complete and obtained a slope $\alpha = 2.49 \pm 0.15$. This is a bit steeper than the traditional Kroupa slope of $\alpha = 2.3$ (Kroupa 2001) or $\alpha = 2.27 \pm 0.08$ measured in the λ Ori association (Barrado y Navascues et al. 2004),

El.	This work					GALAH DR3		
	$\varepsilon(X)$	$\varepsilon(X)$	$\left[\frac{X}{Fe}\right]$	$\left[\frac{X}{Fe}\right]$	stat. un- certainty	notes	$\varepsilon(X)$	$\left[\frac{X}{Fe}\right]$
	mean normalised	5770 K normalised	mean normalised	5770 K normalised			mean normalised	mean normalised
Li	3.41	3.55	2.36	2.50	0.123		3.00 ± 0.10	1.96 ± 0.10
O	9.76	9.04	1.07	0.35	0.063	1	9.50 ± 0.14	0.81 ± 0.14
Na	6.02	6.33	-0.21	0.09	0.025		6.14 ± 0.06	-0.08 ± 0.06
Mg	7.57	7.64	-0.02	0.04	0.040		7.48 ± 0.09	-0.12 ± 0.08
Al	6.47	6.51	0.02	0.06	0.027		6.40 ± 0.08	-0.03 ± 0.08
Si	7.45	7.37	-0.05	-0.13	0.081		7.56 ± 0.06	0.05 ± 0.07
K	5.20	5.87	0.17	0.84	0.035		5.35 ± 0.10	0.27 ± 0.09
Ca	6.36	6.68	0.02	0.34	0.032		6.50 ± 0.08	0.19 ± 0.08
Sc	3.13	3.24	-0.01	0.09	0.043		3.05 ± 0.07	-0.11 ± 0.06
Ti	4.70	4.56	-0.24	-0.38	0.053		5.00 ± 0.08	0.06 ± 0.07
V	3.94	3.91	0.01	-0.01	0.027	2	3.98 ± 0.11	0.03 ± 0.10
Cr	5.41	5.24	-0.22	-0.39	0.054		5.64 ± 0.10	0.04 ± 0.09
Mn	5.23	5.47	-0.19	0.04	0.049		5.42 ± 0.09	0.03 ± 0.08
Fe*	7.34	7.39	-0.15	-0.10	0.016		7.48 ± 0.07	-0.02 ± 0.07
Co	4.97	4.99	-0.01	0.00	0.069	2	5.05 ± 0.11	-0.03 ± 0.11
Ni	6.39	6.26	0.17	0.04	0.029		6.19 ± 0.10	-0.08 ± 0.09
Cu	3.59	3.65	-0.59	-0.53	0.029		4.02 ± 0.08	-0.20 ± 0.08
Zn	3.86	3.99	-0.69	-0.56	0.101		4.62 ± 0.13	0.09 ± 0.13
Rb	3.38	3.76	0.86	1.24	0.097	1	2.63 ± 0.13	0.018 ± 0.14
Y	2.12	1.82	-0.08	-0.38	0.126	1, 3	2.50 ± 0.17	0.38 ± 0.17
Zr	2.08	1.70	-0.49	-0.87	0.157	1, 2	2.90 ± 0.14	0.22 ± 0.13
Ba	1.91	2.16	-0.26	-0.01	0.029		2.54 ± 0.10	0.39 ± 0.09
Ce	2.29	1.67	0.71	0.09	0.214	1	1.80 ± 0.21	0.28 ± 0.21
Nd	0.37	0.37	-1.04	-1.04	0.099		2.42 ± 0.11	1.02 ± 0.11
Eu	0.43	0.49	-0.08	-0.02	0.057		1.07 ± 0.09	0.54 ± 0.09

¹ Large range

² Colder stars dominate

³ Hotter stars dominate

* $[Fe/H]$ instead of $[X/Fe]$ is given in 4th and 5th columns

Table 3. Absolute abundances of 25 elements. “Large range” means that the abundance measurements are spread over a large range (> 1 dex) before detrending, so the systematic uncertainty is large. This implies that the reported absolute abundances are unreliable. Some elements have the measurements dominated by cold (note 2) or hot stars (note 3), so the mean is not calculated over the same type of stars for all elements. “Mean normalised” abundances were detrended so the mean remained the same after detrending. “5770 K normalised” abundances were detrended so the value at 5770 K (Solar T_{eff}) remained the same.

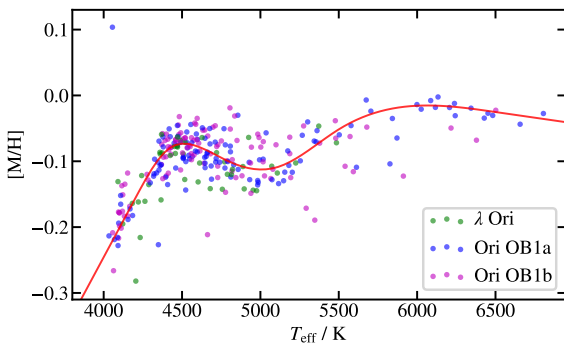


Figure 9. Measured mean metallicities for each star as a function of effective temperature. A clear trend exists and is independent of the cluster or region in the Orion complex. Solid line shows a cubic spline fit to the trend.

$\alpha = 2.40 \pm 0.09$ in 25 Ori cluster (Suárez et al. 2019), $\alpha = 2.4 \pm$ in the ONC (De Marchi et al. 2005), $\alpha = 2.21 \pm 0.18$ in the Trapezium cluster (Muench et al. 2002), but flatter than $\alpha = 2.7$ in the ONC and the Trapezium cluster Pflamm-Altenburg & Kroupa (2006), $\alpha = 2.9 \pm 0.2$ in the ONC and the λ Ori association or $\alpha = 3.0 \pm 0.1$ in the σ Ori cluster (De Marchi et al. 2010).

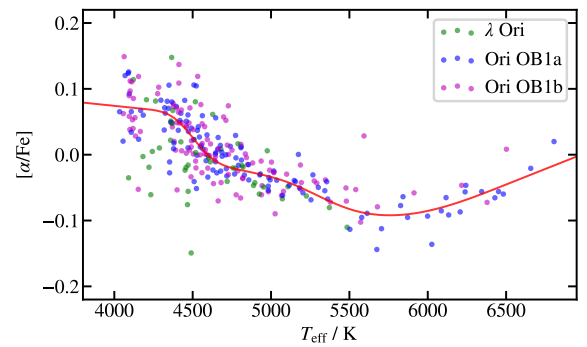


Figure 10. Measured mean alpha abundance for each star as a function of effective temperature. A clear trend exists and is independent of the cluster or region in the Orion complex. Solid line shows a cubic spline fit to the trend.

We use data from Portinari et al. (1998) to estimate lifetimes of stars as a function of stellar mass. A function

$$\tau(m) = \left[3.171 \left(\frac{m}{M_{\odot}} \right)^{-2.178} - 1.151 \cdot 10^{-5} \left(\frac{m}{M_{\odot}} \right) + 0.00443 \right] \text{ Gyr} \quad (5)$$

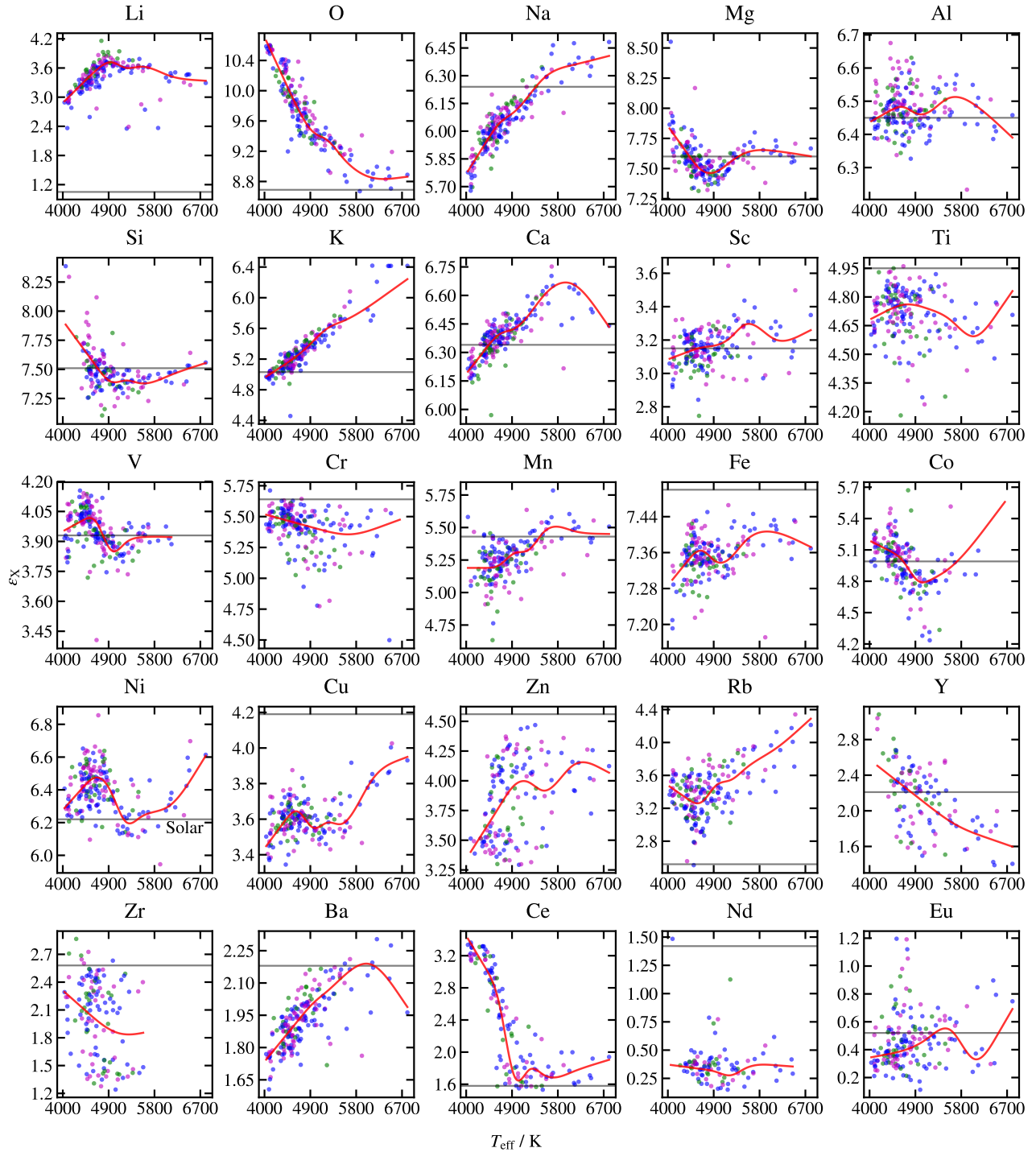


Figure 11. Measured mean abundances of 25 elements for each star as a function of effective temperature. A clear trend exists for most elements and is independent of the cluster or region in the Orion complex. Solid red line shows a cubic spline fit to the trend. Horizontal line shows the Solar abundance from [Asplund et al. \(2009\)](#).

describes the relation well for massive stars and $[M/H] = -0.07$. By using our ages of clusters and extrapolating and integrating the IMF, we estimate that in the observed population there were between 0.81 and 2.28 (for α between 2.64 and 2.34) core collapse SNe in the population studied in this paper. This number drops to 0.23 – 0.73 SNe, if we only consider time until 7 Myr ago when the last clusters formed. These estimates do not include any runaway/ejected stars

into the IMF, so the actual number is a fraction higher. Assuming a steeper IMF, sometimes quoted in the literature listed above, the number of SNe drops to essentially zero. A much flatter IMF (lets say $\alpha = 1.8$), which is not excluded by most massive stars ($m > 5M_{\odot}$) and is not unprecedented in the literature ([De Marchi et al. 2005](#); [Bastian et al. 2010](#)), would produce around ten times more SNe

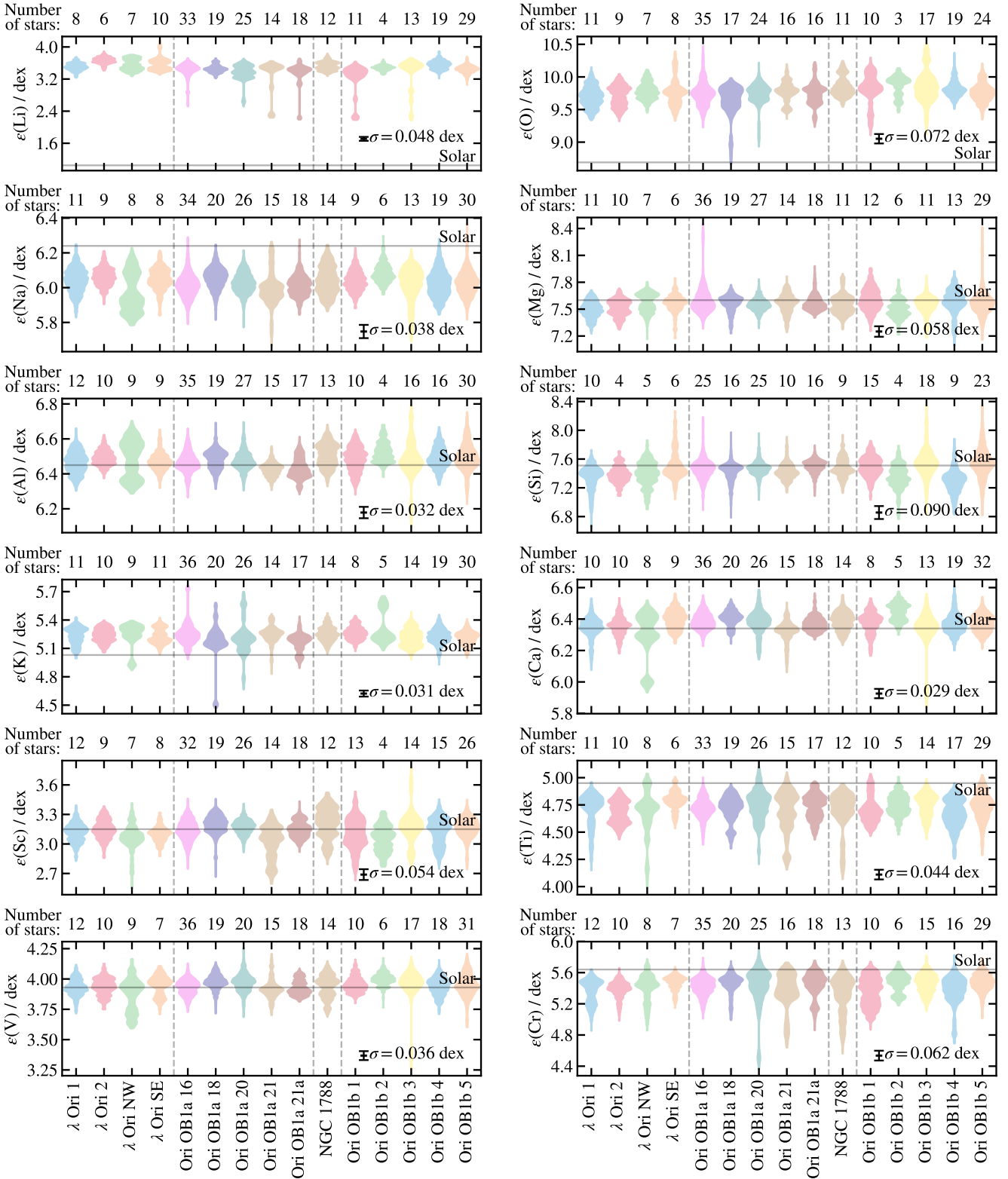


Figure 12. Caption

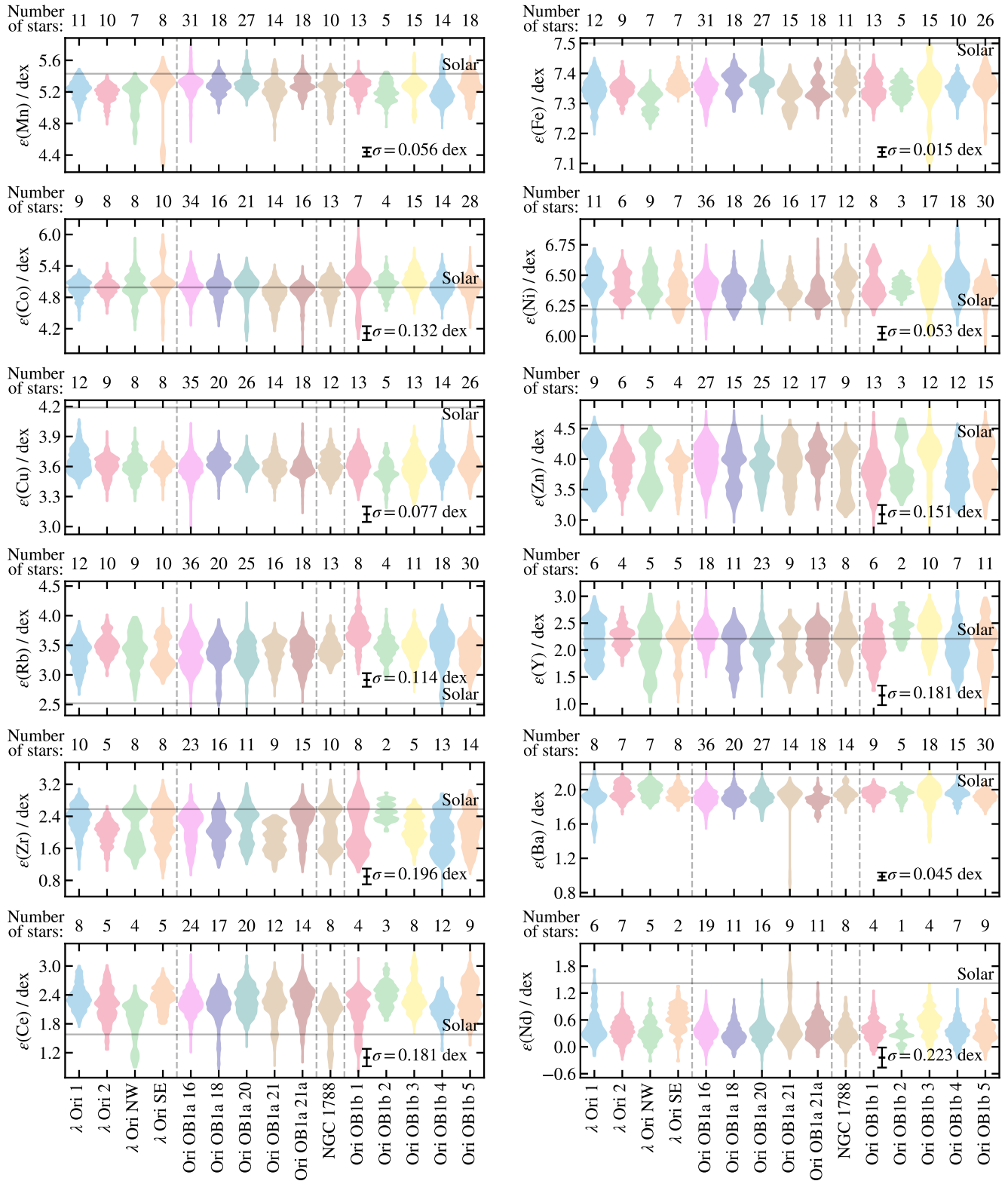


Figure 12. contd.

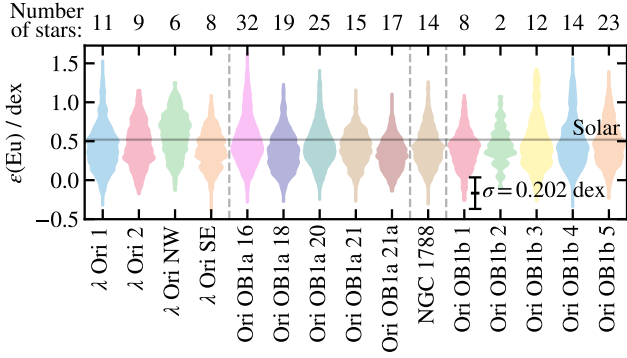


Figure 12. contd.

than an IMF with $\alpha = 2.49$. However, we do not expect that such an extrapolation is realistic.

From the observation of chemical homogeneity we can deduce how many SNe would have to pollute the ISM for younger clusters to show different chemical abundances. In the following estimate we neglect any physics of ISM mixing, as this is out of the scope of this paper. We only deal with net yields of core collapse supernovae and observed abundances. From Figure 8 we can see that the largest alpha enhancement are 0.03 dex in the λ Ori NW and 0.02 dex in Ori OB1b 1 clusters. However, these two clusters are unlikely to be polluted due to supernova explosions originating in older clusters; λ Ori is too far from old clusters in Ori OB1a and cluster Ori OB1b 1 is too old and was most likely formed before any supernova explosion took place in the Orion complex. A typical core-collapse supernova with initial mass of $25 M_{\odot}$ produces $4 M_{\odot}$ of alpha elements (Nomoto et al. 2006). Our largest clusters have masses of around $600 M_{\odot}$. Assuming a star formation efficiency of 0.3 (Da Rio et al. 2014), our clusters are formed from gas clouds of around $2000 M_{\odot}$. Ejecta from one $25 M_{\odot}$ supernova, if completely and ideally mixed with such cloud, enhance its alpha abundance by 0.05 dex, which would be detectable in our observations. Individual abundances of Cr, Mg, and Si would increase for 0.06 dex, Ti for 0.02 dex and Oxygen by 0.03 to 0.08 dex, depending which absolute abundance from Table 3 is used. We measure Oxygen abundances from the 777 nm Oxygen triplet. These are the only Oxygen lines in HERMES’ spectral range and are also lines with the highest excitation potential of all fitted lines. They are known to be very sensitive to non LTE effects, chromospheric activity and atmospheric models of young stars (Morel & Micela 2004; Schuler et al. 2006; Shen et al. 2007). As a result our Oxygen abundances are significantly higher than in the existing literature (Cunha & Lambert 1992, 1994; Cunha et al. 1998). Because the temperature trend (see Figure 11) is well behaved, we still use Oxygen as a tracer of chemical homogeneity, but any absolute Oxygen abundances given in this paper are invalid. Lack of any observed chemical enrichment can be explained either by no supernovae in the studied population during the star formation phase, inefficient mixing and directed flows, or large distance between the supernova and star forming regions. We can claim with high certainty that the number of SNe in the Orion complex was not high, as this would be reflected in chemical inhomogeneities.

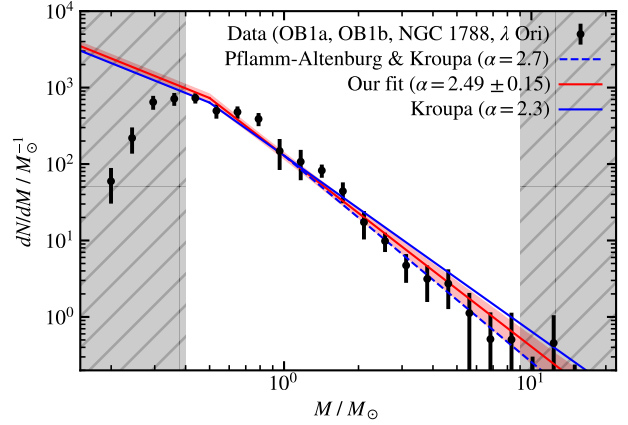


Figure 13. Estimation of the IMF of the Orion complex. Selection function is described in Section 5 and is different from the selection function used for clustering. Selection is not complete in shaded regions. A traditional Kroupa IMF shown with a solid blue line (Kroupa 2001) and an IMF obtained for massive stars by Pflamm-Altenburg & Kroupa (2006) shown with a dashed blue line are given as a reference. Our fit with 1σ uncertainty is shown in red.

6 CONCLUSIONS AND DISCUSSION

Our conclusions are based on Ori OB1a, OB1b, λ Ori and NGC 1788 regions. We did not observe the ONC or σ Ori regions due to several concerns. These are the regions with the largest differential reddening, which we have no way of properly accounting for. This would result in poorly fitted isochrones and consequently inaccurate photometric temperature and gravity. We did not analyse how this would impact our spectroscopic analysis, but our approach would definitely had to be revised to include younger stars and clusters with strong differential reddening. Stars that we included into the analysis are either main sequence stars or PMS stars very close to the main sequence. Stars < 5 Myr old, like the ones in ONC and σ Ori regions would be PMS stars, lying well above the main sequence and we had concerns that synthetic model codes would not perform well enough for them. This could make calculation of precise relative abundances hard and we would not be able to interpret properly any observed chemical differences. However, we did observe one star that is more likely to belong to the σ Ori cluster and has well determined atmospheric parameters and abundances. It is chemically identical to other stars from this work.

Number of supernovae exploded to date in the Orion complex is a highly debated topic. Bubble-like structures (Barnard’s loop, Orion-Eridanus superbubble, λ Orion bubble) were most likely made by supernova explosions, but the present structure suggests that stellar winds played a significant role (Ochsendorf et al. 2015) as well and formed rich substructure. Expanding velocity of the bubbles can be used as an indicator when they were formed – but such estimates are inaccurate (Bally 2008) and cannot provide the exact time of the supernovae explosions. Brown et al. (1995) estimate the age of the largest bubble – Orion Eridanus superbubble is between 1.8 and 5.3 Myr. This suggests that the bubbles are a product of recent supernovae explosions (as opposed to the age of the stellar population studied in this paper). Low number of supernovae in the Orion complex is also supported by a shortfall of supernovae remnants. G203.2 - 12.3 is the only supernova remnant classified in Orion (possibly observed in 483 CE) (Winkler & Reipurth 1992). Another indirect tracer is emission from the radioactive decay of

^{26}Al in Ori OB1a (Voss et al. 2010; Schlafly et al. 2015). Models of SN and stellar wind feedbacks by Voss et al. (2010) suggest that ^{26}Al was produced by few recent supernovae. ^{60}Fe is another radioactive tracer of SN (Wang et al. 2020), which has not been explored yet in the Orion complex.

We show that most probably there were none or at least very few supernovae explosions in the early stages of the Orion complex formation. Young supernova remnants, also in the form of gas bubbles, can be explained by recent supernovae in the past few million years. Such supernovae could not have chemically polluted the ISM from which the stars observable today were born.

A convincing way of proving chemical homogeneity of clusters is a direct comparison of spectra (Bovy 2016). The method avoids calculating atmospheric parameters and deriving exact chemical abundances. In our case the parameter space is too large and we would struggle finding spectra with similar atmospheric parameters in order to compare lines of interesting elements. One of the reasons this is hardly possible in young stellar associations as compared to old open clusters is that the stellar rotation takes a large range of values, which effectively adds another dimension of atmospheric parameters. Another drawback is that clusters of different ages would have to be compared, complicating the case for direct spectral comparison even further.

ACKNOWLEDGEMENTS

This work is based on data acquired through the Australian Astronomical Observatory, under programmes: A/2019A/01 (Hierarchical star formation in Ori OB1), A/2014A/25, A/2015A/19, A2017A/18 (The GALAH survey); A/2015A/03, A/2015B/19, A/2016A/22, A/2016B/12, A/2017A/14 (The K2-HERMES K2-follow-up program); A/2016B/10 (The HERMES-TESS program); A/2015B/01 (Accurate physical parameters of Kepler K2 planet search targets); S/2015A/012 (Planets in clusters with K2). We acknowledge the traditional owners of the land on which the AAT stands, the Gamilaraay people, and pay our respects to elders past and present. This work has made use of data from the European Space Agency (ESA) mission *Gaia* (<https://www.cosmos.esa.int/gaia>), processed by the *Gaia* Data Processing and Analysis Consortium (DPAC, <https://www.cosmos.esa.int/web/gaia/dpac/consortium>). Funding for the DPAC has been provided by national institutions, in particular the institutions participating in the *Gaia* Multilateral Agreement.

REFERENCES

- Alves J., Bouy H., 2012, *A&A*, **547**, A97
- Asplund M., Grevesse N., Sauval A. J., Scott P., 2009, *ARA&A*, **47**, 481
- Bailer-Jones C. A. L., Rybizki J., Fouesneau M., Mantelet G., Andrae R., 2018, *AJ*, **156**, 58
- Bally J., 2008, Overview of the Orion Complex. p. 459
- Barrado y Navascues D., Stauffer J. R., Bouvier J., 2004, arXiv e-prints, pp astro-ph/0409499
- Basri G., Marcy G. W., Valenti J. A., 1992, *ApJ*, **390**, 622
- Bastian N., Covey K. R., Meyer M. R., 2010, *ARA&A*, **48**, 339
- Biazzo K., Randich S., Palla F., 2011a, *A&A*, **525**, A35
- Biazzo K., Randich S., Palla F., Briceño C., 2011b, *A&A*, **530**, A19
- Blanco-Cuaresma S., 2019, *MNRAS*, **486**, 2075
- Blanco-Cuaresma S., Soubiran C., Heiter U., Jofré P., 2014, *A&A*, **569**, A111
- Bovy J., 2016, *ApJ*, **817**, 49
- Bressan A., Marigo P., Girardi L., Salasnich B., Dal Cero C., Rubele S., Nanni A., 2012, *MNRAS*, **427**, 127
- Brown A. G. A., Hartmann D., Burton W. B., 1995, *A&A*, **300**, 903
- Buder S., et al., 2018, *MNRAS*, **478**, 4513
- Carter B. D., 1989, Proceedings of the Astronomical Society of Australia, **8**, 68
- Casamiquela L., Tarricq Y., Soubiran C., Blanco-Cuaresma S., Jofré P., Heiter U., Tucci Maia M., 2019, arXiv e-prints, p. arXiv:1912.08539
- Chen Y., Girardi L., Bressan A., Marigo P., Barbieri M., Kong X., 2014, *MNRAS*, **444**, 2525
- Chen B., D’Onghia E., Alves J., Adamo A., 2019, arXiv e-prints, p. arXiv:1905.11429
- Cottle J. N., et al., 2018, *ApJS*, **236**, 27
- Cunha K., Lambert D. L., 1992, *ApJ*, **399**, 586
- Cunha K., Lambert D. L., 1994, *ApJ*, **426**, 170
- Cunha K., Smith V. V., Lambert D. L., 1995, *ApJ*, **452**, 634
- Cunha K., Smith V. V., Lambert D. L., 1998, *ApJ*, **493**, 195
- Da Rio N., Tan J. C., Jaehnig K., 2014, *ApJ*, **795**, 55
- De Marchi G., Paresce F., Portegies Zwart S., 2005, The Stellar IMF of Galactic Clusters and Its Evolution. p. 77, doi:10.1007/978-1-4020-3407-7_11
- De Marchi G., Paresce F., Portegies Zwart S., 2010, *ApJ*, **718**, 105
- Fang M., et al., 2017, *AJ*, **153**, 188
- Foreman-Mackey D., Hogg D. W., Lang D., Goodman J., 2013, *PASP*, **125**, 306
- Jofré P., et al., 2014, *A&A*, **564**, A133
- Johns-Krull C. M., Valenti J. A., Koresko C., 1999, *ApJ*, **516**, 900
- Kos J., et al., 2017, *MNRAS*, **464**, 1259
- Kos J., et al., 2019, *A&A*, **631**, A166
- Kounkel M., Hartmann L., Calvet N., Megeath T., 2017, *AJ*, **154**, 29
- Kounkel M., et al., 2018, *AJ*, **156**, 84
- Kroupa P., 2001, *MNRAS*, **322**, 231
- Maíz Apellániz J., Weiler M., 2018, *A&A*, **619**, A180
- Morel T., Micela G., 2004, *A&A*, **423**, 677
- Muench A. A., Lada E. A., Lada C. J., Alves J., 2002, *ApJ*, **573**, 366
- Nomoto K., Tominaga N., Umeda H., Kobayashi C., Maeda K., 2006, *Nuclear Phys. A*, **777**, 424
- Ochsendorf B. B., Brown A. G. A., Bally J., Tielens A. G. G. M., 2015, *ApJ*, **808**, 111
- Pflamm-Altenburg J., Kroupa P., 2006, *Monthly Notices of the Royal Astronomical Society*, **373**, 295
- Piskunov N., Valenti J. A., 2017, *A&A*, **597**, A16
- Portinari L., Chiosi C., Bressan A., 1998, *A&A*, **334**, 505
- Schlafly E. F., et al., 2015, *ApJ*, **799**, 116
- Schuler S. C., King J. R., Terndrup D. M., Pinsonneault M. H., Murray N., Hobbs L. M., 2006, *ApJ*, **636**, 432
- Sharma S., Johnston K. V., 2009, *ApJ*, **703**, 1061
- Shen Z. X., Liu X. W., Zhang H. W., Jones B., Lin D. N. C., 2007, *ApJ*, **660**, 712
- Simón-Díaz S., 2010, *A&A*, **510**, A22
- Suárez G., Downes J. J., Román-Zúñiga C., Cerviño M., Briceño C., Petr-Gotzens M. G., Vivas K., 2019, *MNRAS*, **486**, 1718
- Tang J., Bressan A., Rosenfield P., Slemmer A., Marigo P., Girardi L., Bianchi L., 2014, *MNRAS*, **445**, 4287
- Valenti J. A., Piskunov N., 1996, *A&AS*, **118**, 595
- Virtanen P., et al., 2019, arXiv e-prints, p. arXiv:1907.10121
- Voss R., Diehl R., Vink J. S., Hartmann D. H., 2010, *A&A*, **520**, A51
- Wang W., et al., 2020, *ApJ*, **889**, 169
- Winkler P. F., Reipurth B., 1992, *ApJ*, **389**, L25
- Zari E., Brown A. G. A., de Zeeuw P. T., 2019, *A&A*, **628**, A123

APPENDIX A: GRID INTERPOLATION

Figures A1 to A4 demonstrate the interpolation errors introduced by a grid of stellar parameters. Figure A5 shows a small portion of a spectrum and illustrates the differences between synthetic spectra between grid points. A typical fit of two synthetic spectra to an observed spectrum is also displayed.

APPENDIX B: CLUSTERING

Figure B1 shows each cluster in the 6D space (position on the sky, proper motions and parallax).

APPENDIX C: HR DIAGRAMS

Figure C shows HR diagrams for all 15 clusters made with *Gaia* photometry.

APPENDIX D: GALAH DR3 ABUNDANCES

Figure D1 shows mean abundances of 25 elements for a cross-match between our study and GALAH DR3.

This paper has been typeset from a \TeX/L\AA\TeX file prepared by the author.

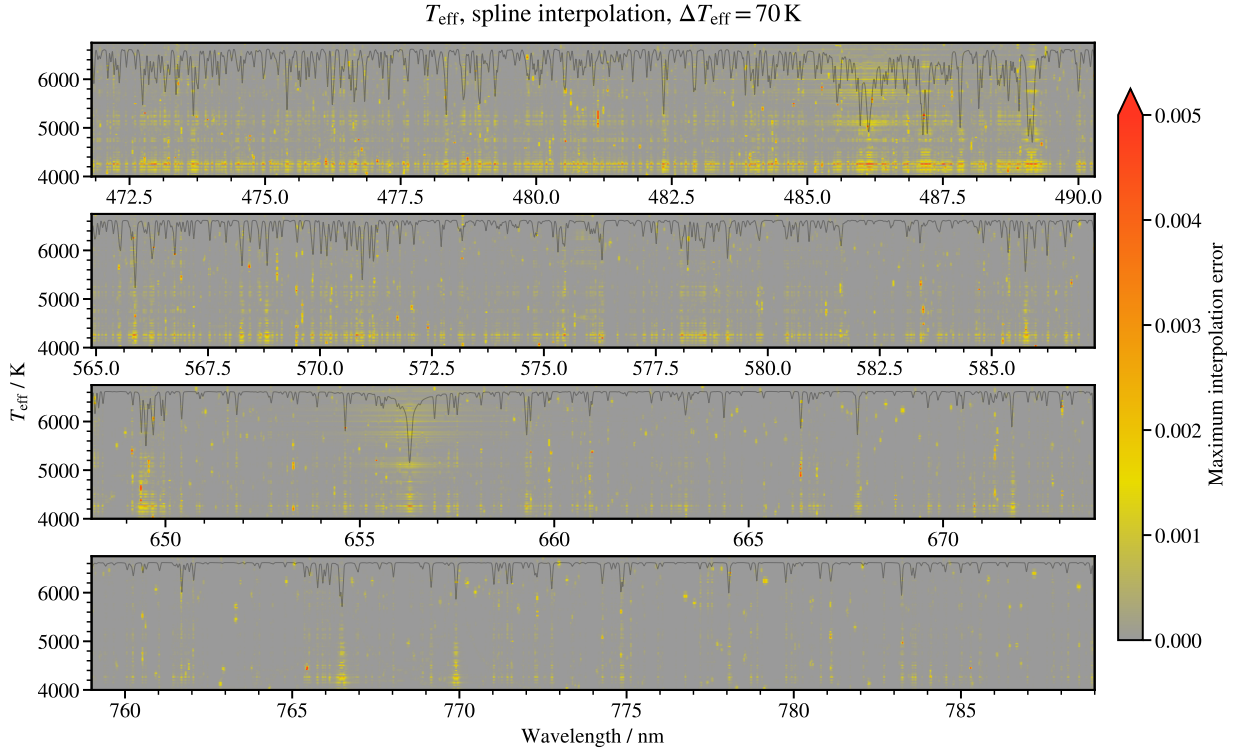


Figure A1. Maximum interpolation error in the T_{eff} dimension of the parameter grid. Colours show the difference between a synthetic spectrum and an interpolated spectrum from a grid. Both spectra are normalized. The interpolated spectrum is always calculated in the middle point between two nodes where the error is expected to be the largest. Errors never exceed the flux of 0.008 (in a normalised spectrum). A spectrum with $T_{\text{eff}} = 5250 \text{ K}$, $\log g = 4.3$, $[M/H] = -0.05$, $[\alpha/Fe] = 0.0$, and $v \sin i = 10 \text{ km s}^{-1}$ is overplotted to illustrate the shape of a typical spectrum.

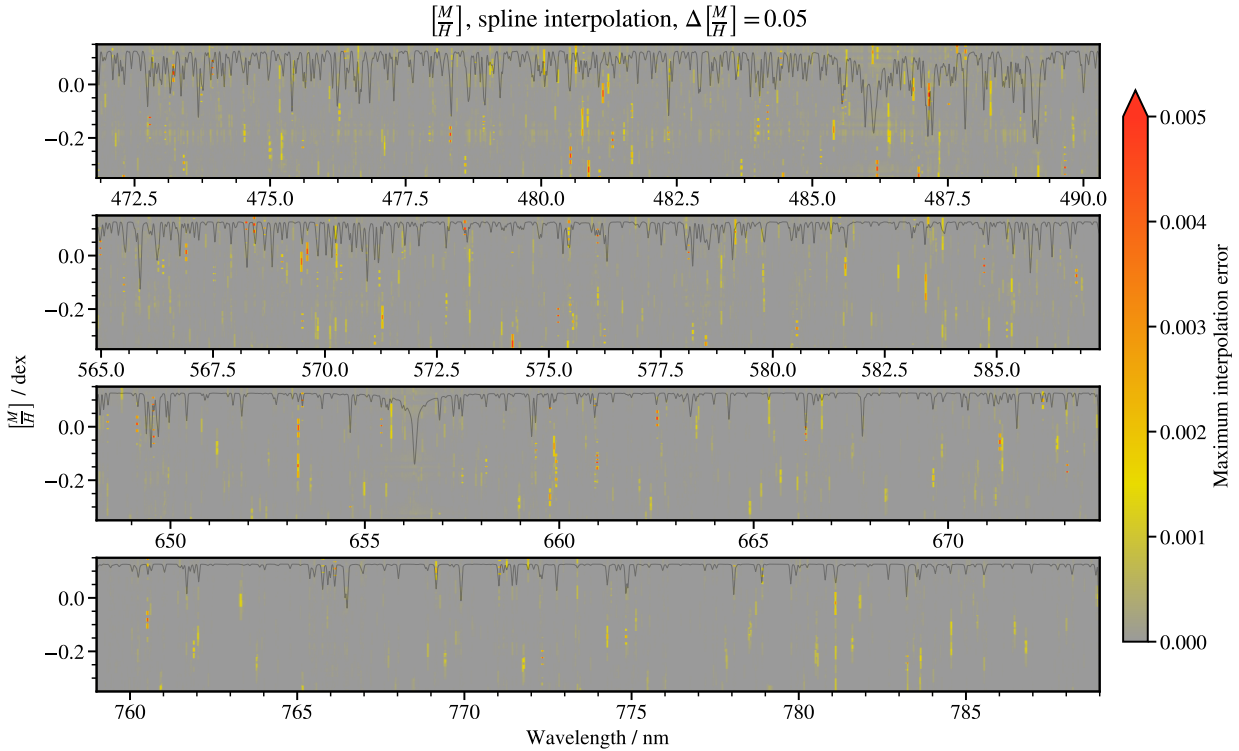


Figure A2. Same as Figure A1 but for metallicity.

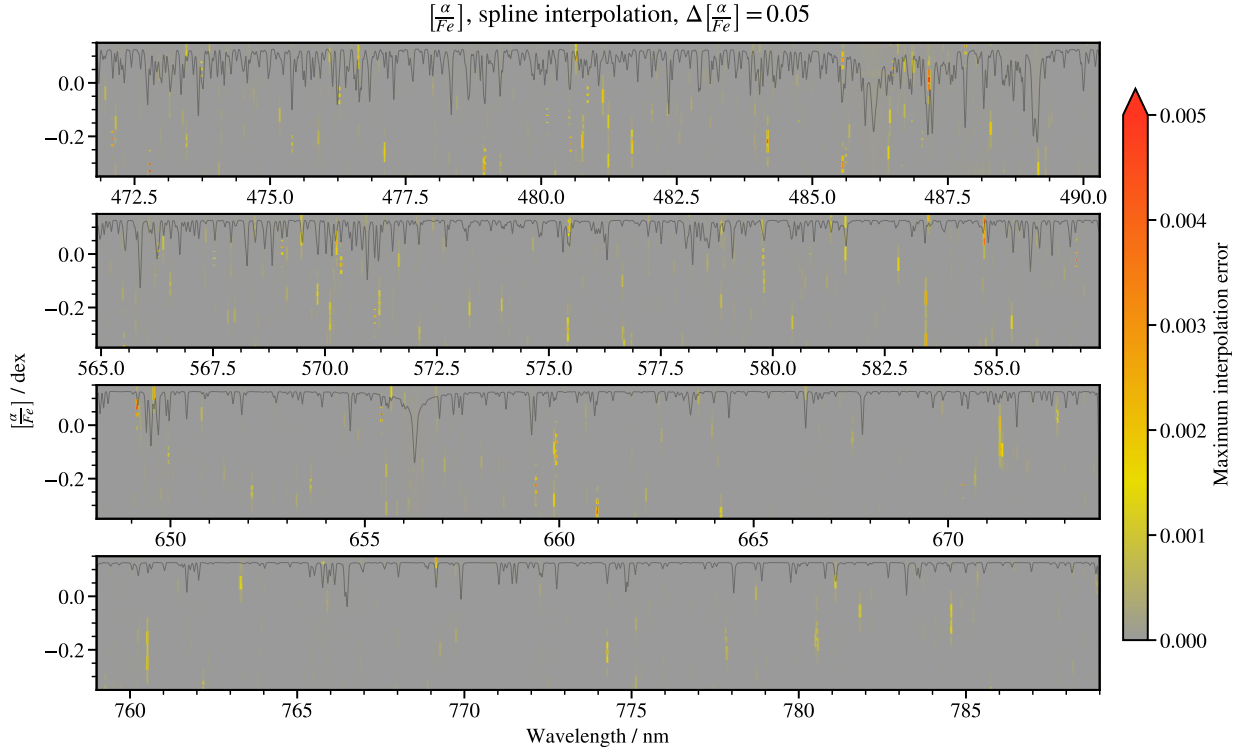


Figure A3. Same as Figure A1 but for α abundance.

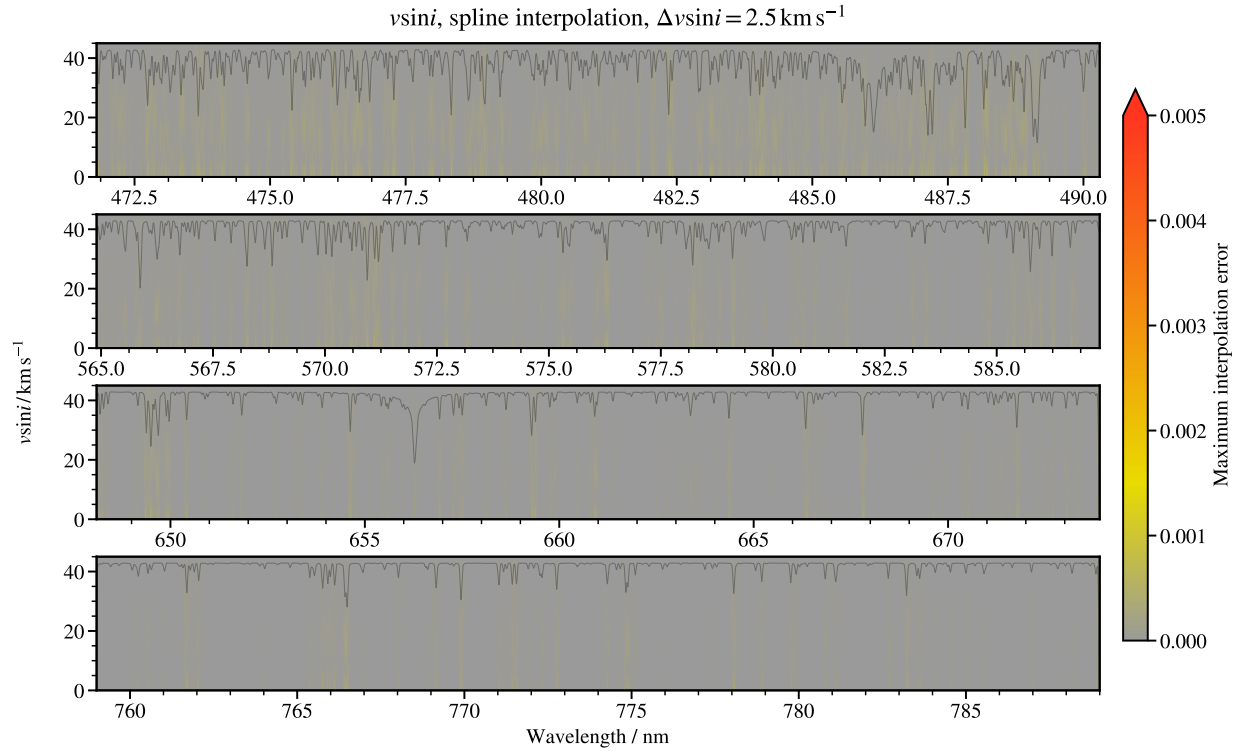


Figure A4. Same as Figure A1 but for $v \sin i$.

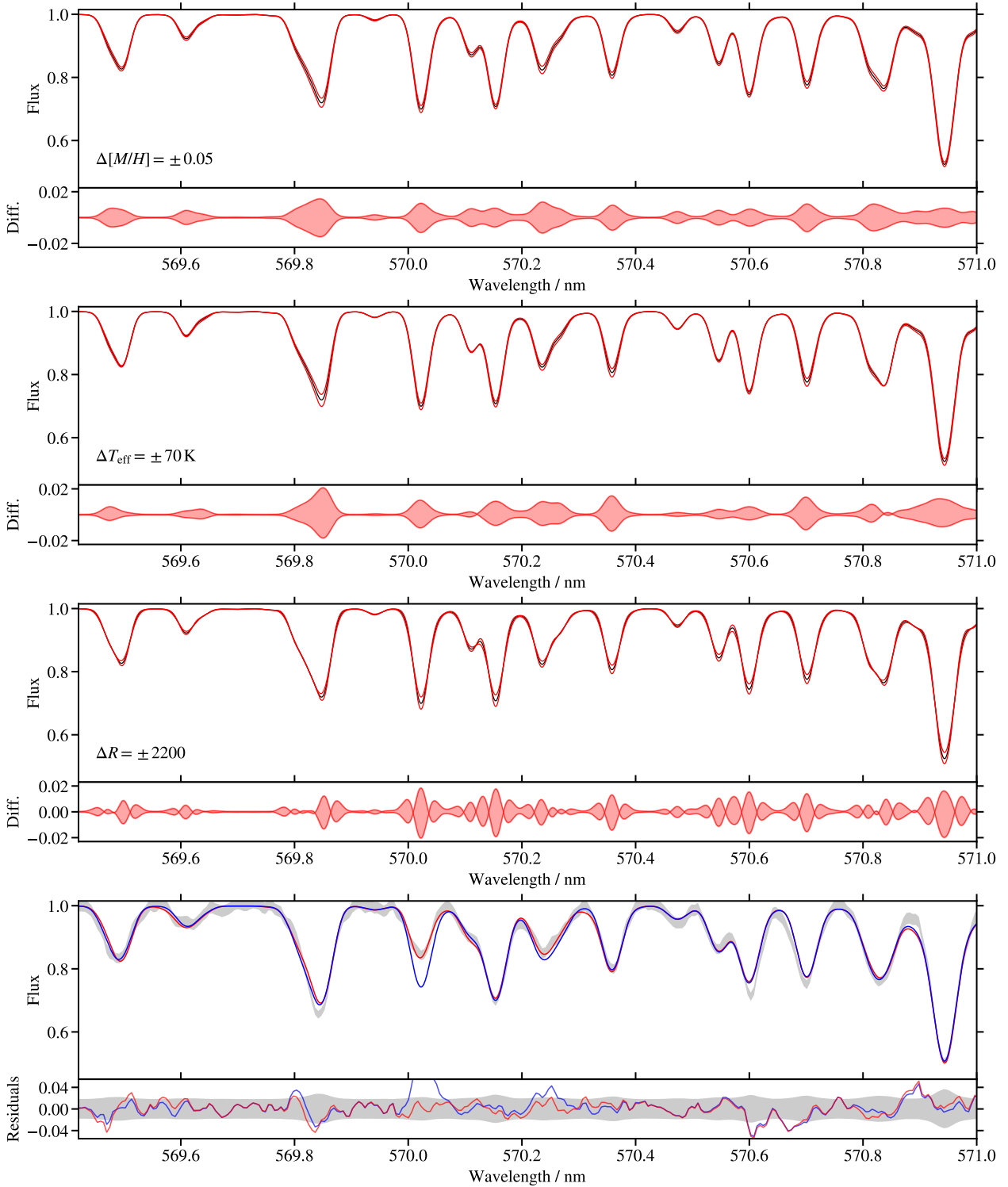


Figure A5. Sensitivity of synthetic templates to small variations in parameters. First panel: red lines show the difference when metallicity is varied for ± 0.05 dex. Black line shows a spectrum with $T_{\text{eff}}=5250$ K, $[M/H]=-0.05$, $[\alpha/Fe]=0.0$, $v \sin i = 5 \text{ km s}^{-1}$, $R = 22000$. Adjacent plot shows the differences between red and black lines in more details. Second panel: red lines show the difference when T_{eff} is varied for ± 70 K. Black line shows the same spectrum as before. Third panel: red lines show the difference when resolving power $R = \lambda/\Delta\lambda$ is varied for 2200. Note how a variation in resolution is not degenerated with variations in $[M/H]$ or T_{eff} . Last panel: Example of an observed spectrum (gray, with thickness corresponding to uncertainty) and best fitting template with a Solar mix of elements (blue). Line at 570.02 nm belongs to Cu I, which has much lower abundance than in the Sun. Since the Solar mix of elements was used in the fit, the fit deviates significantly for this line. Red line shows the fit with Orion-specific mix of elements (see Table 3).

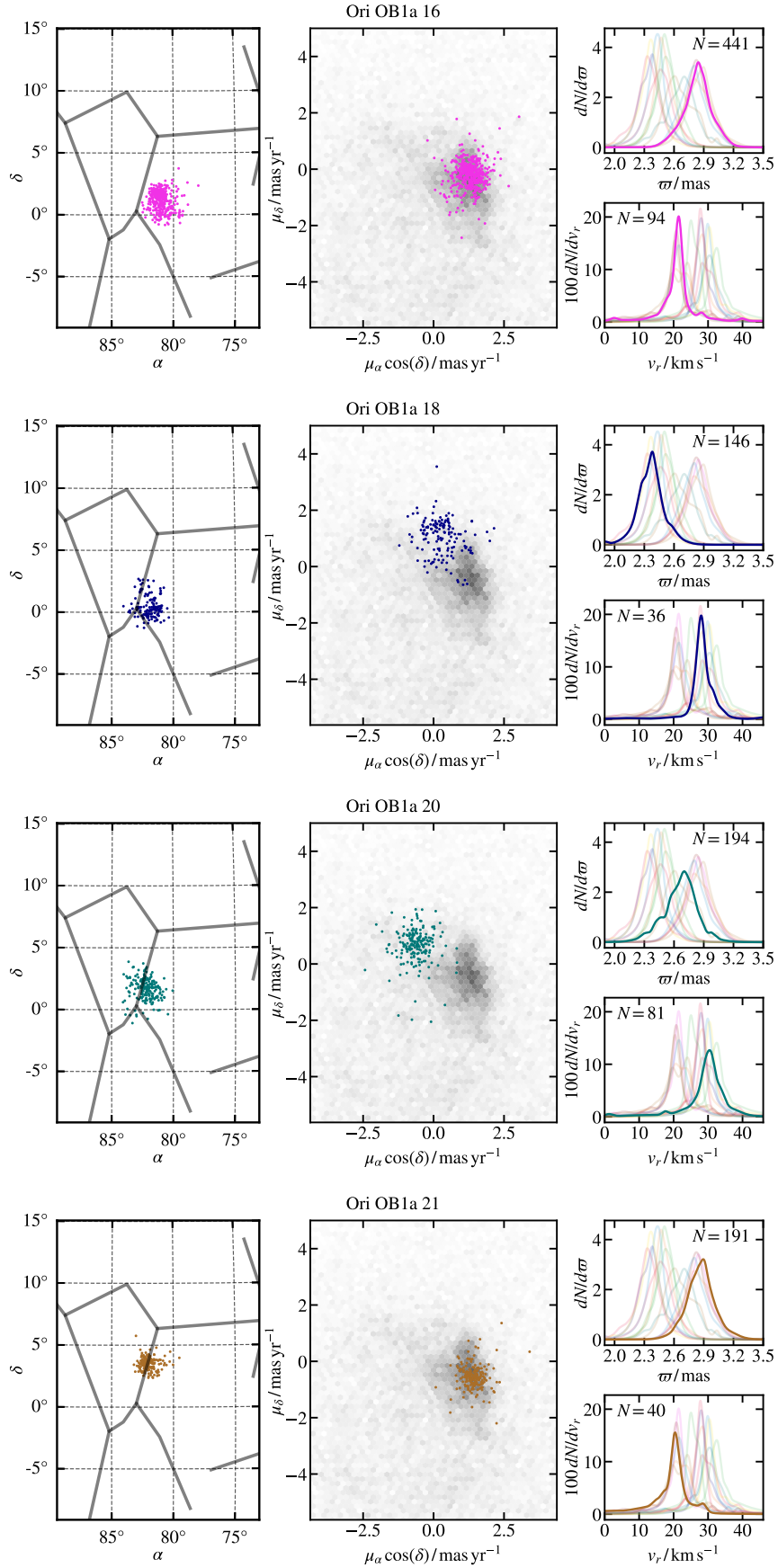


Figure B1. Positions, proper motions, parallax distribution, and radial velocity distribution for all 15 clusters.

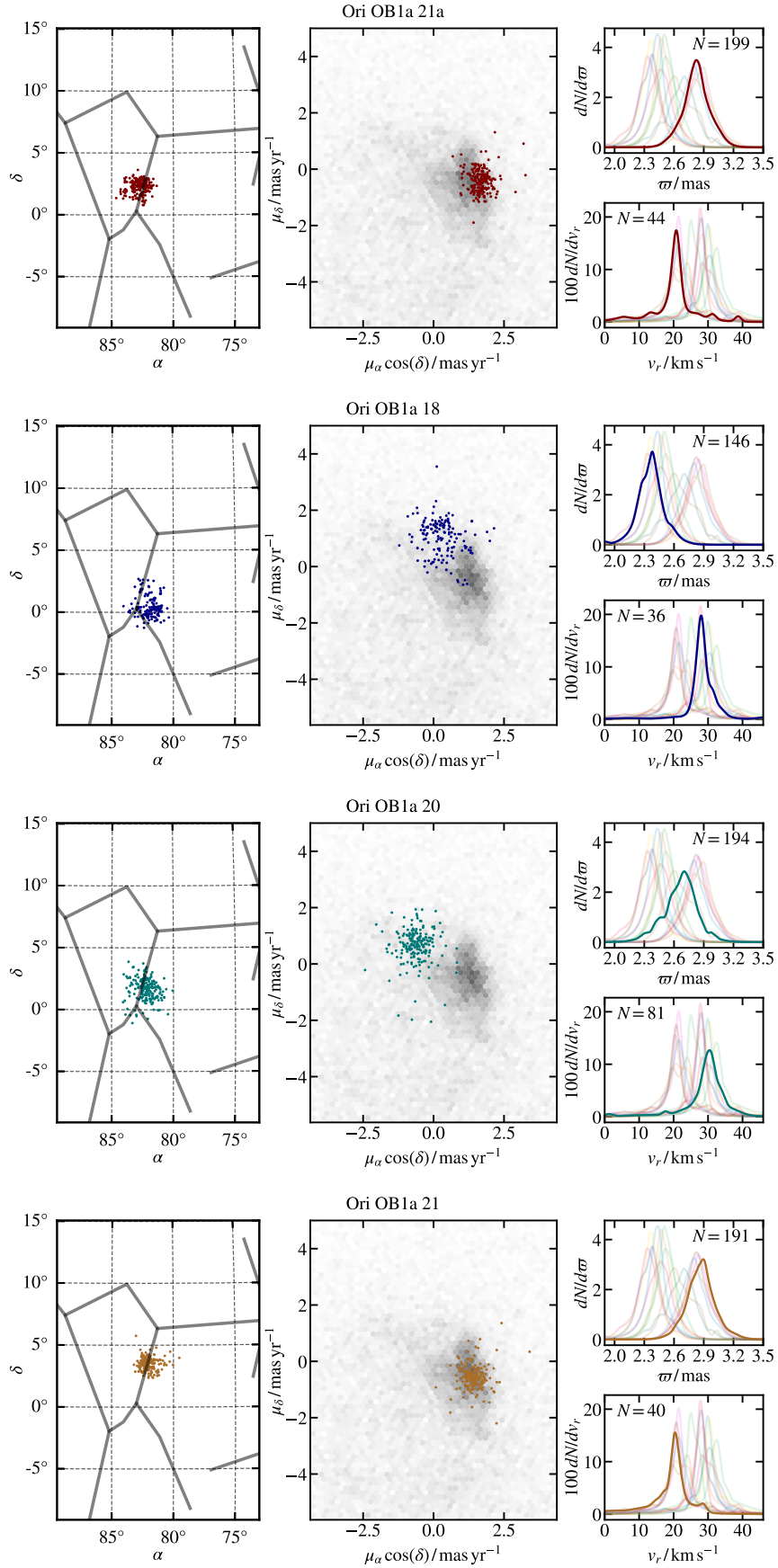


Figure B1. contd.

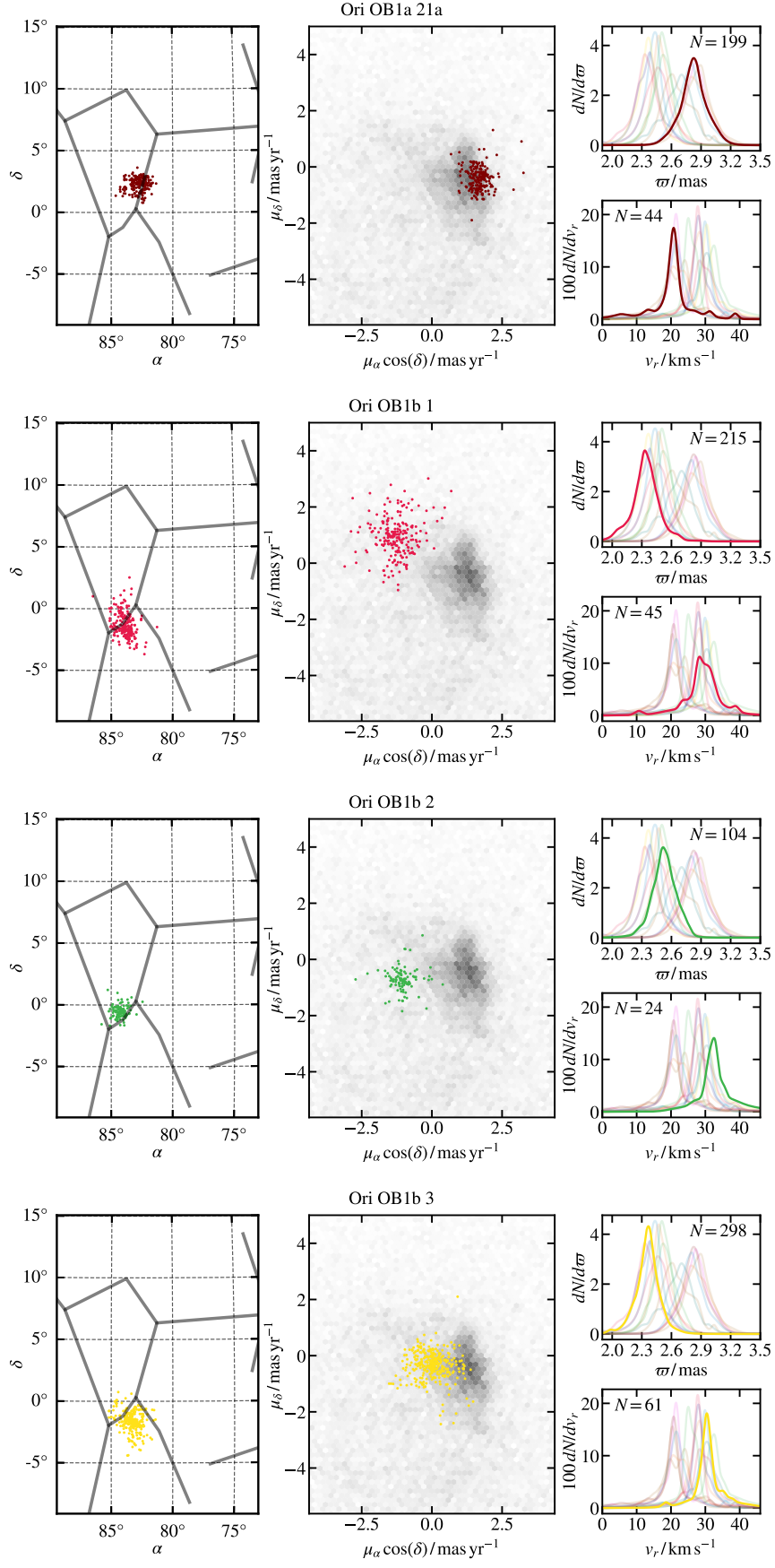


Figure B1. contd.

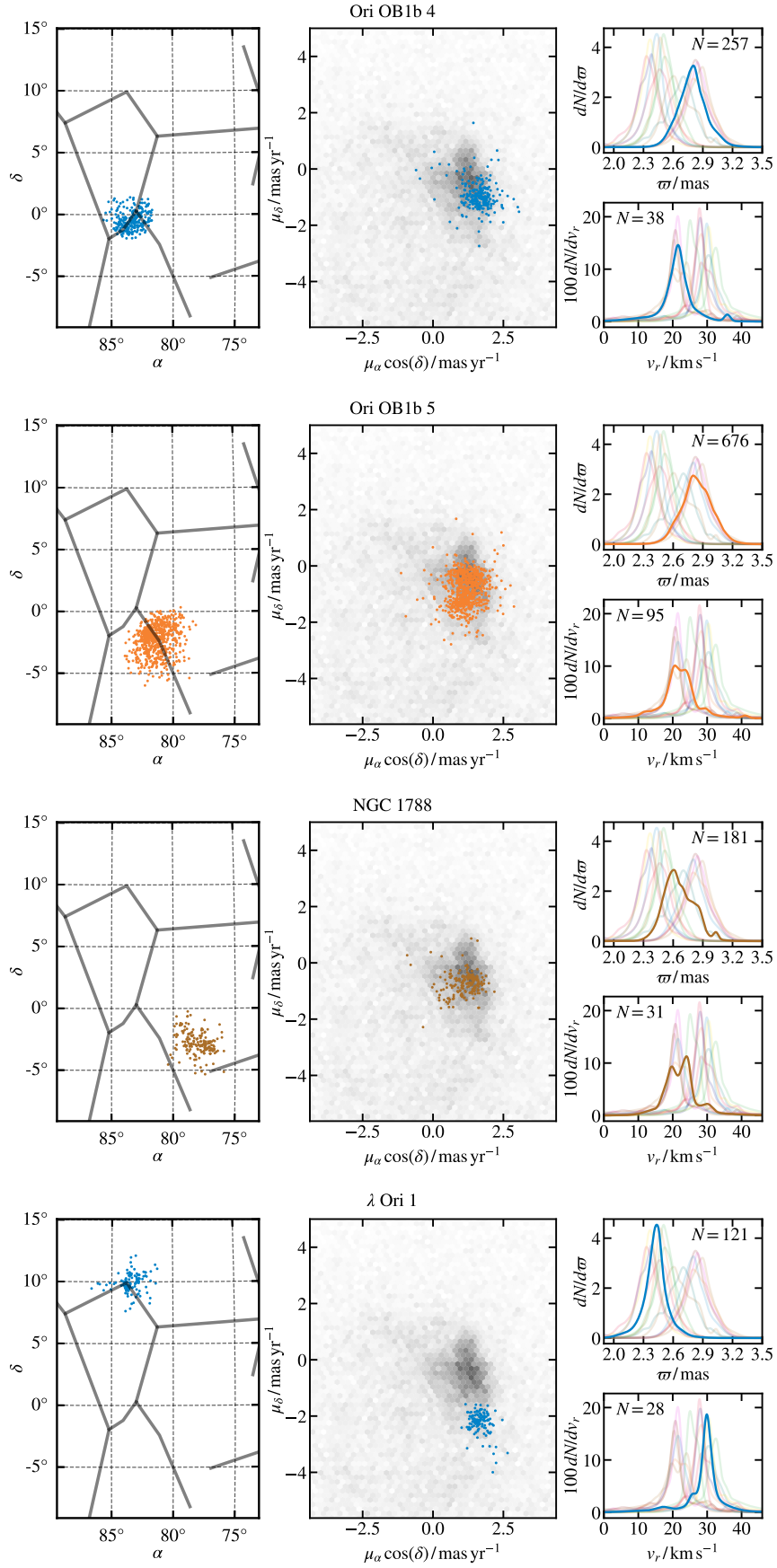


Figure B1. contd.

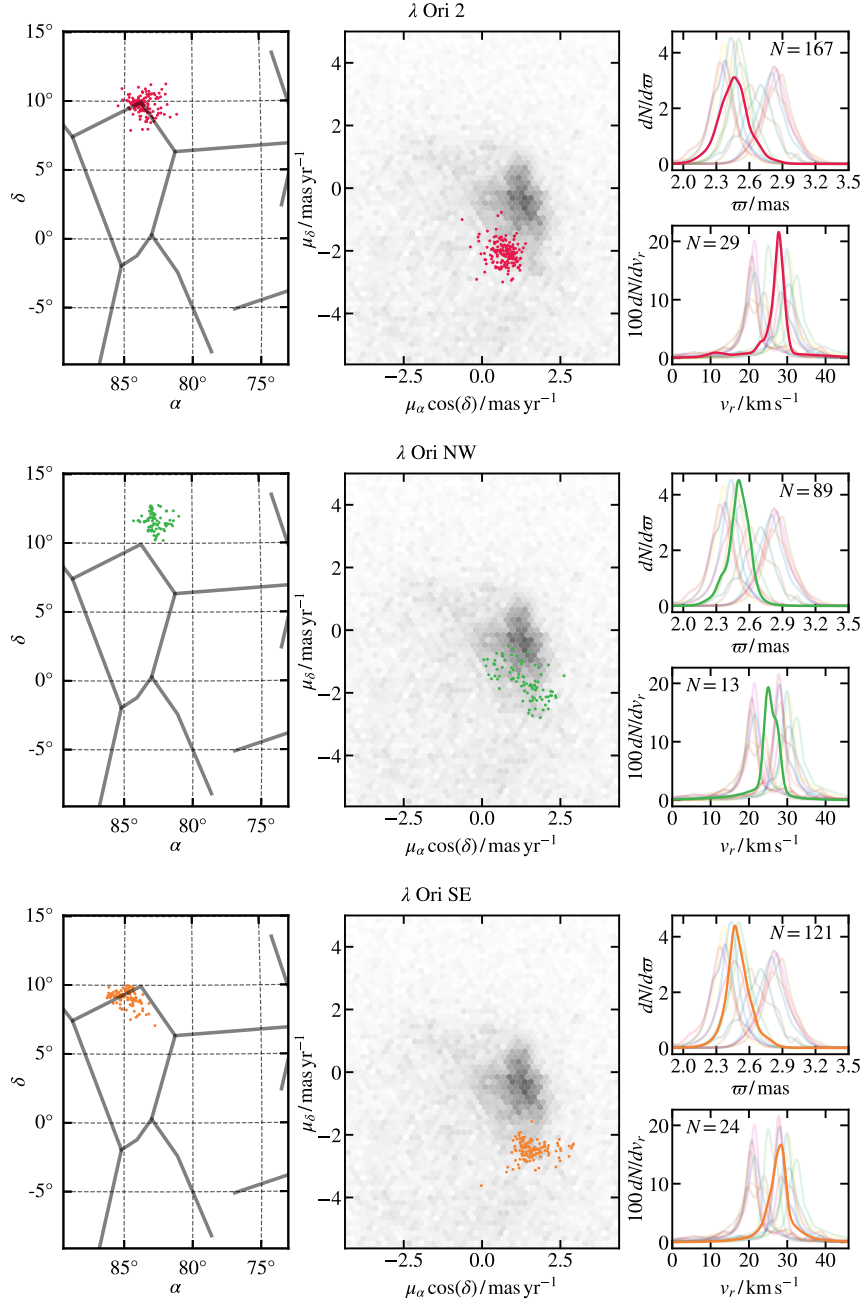


Figure B1. contd.

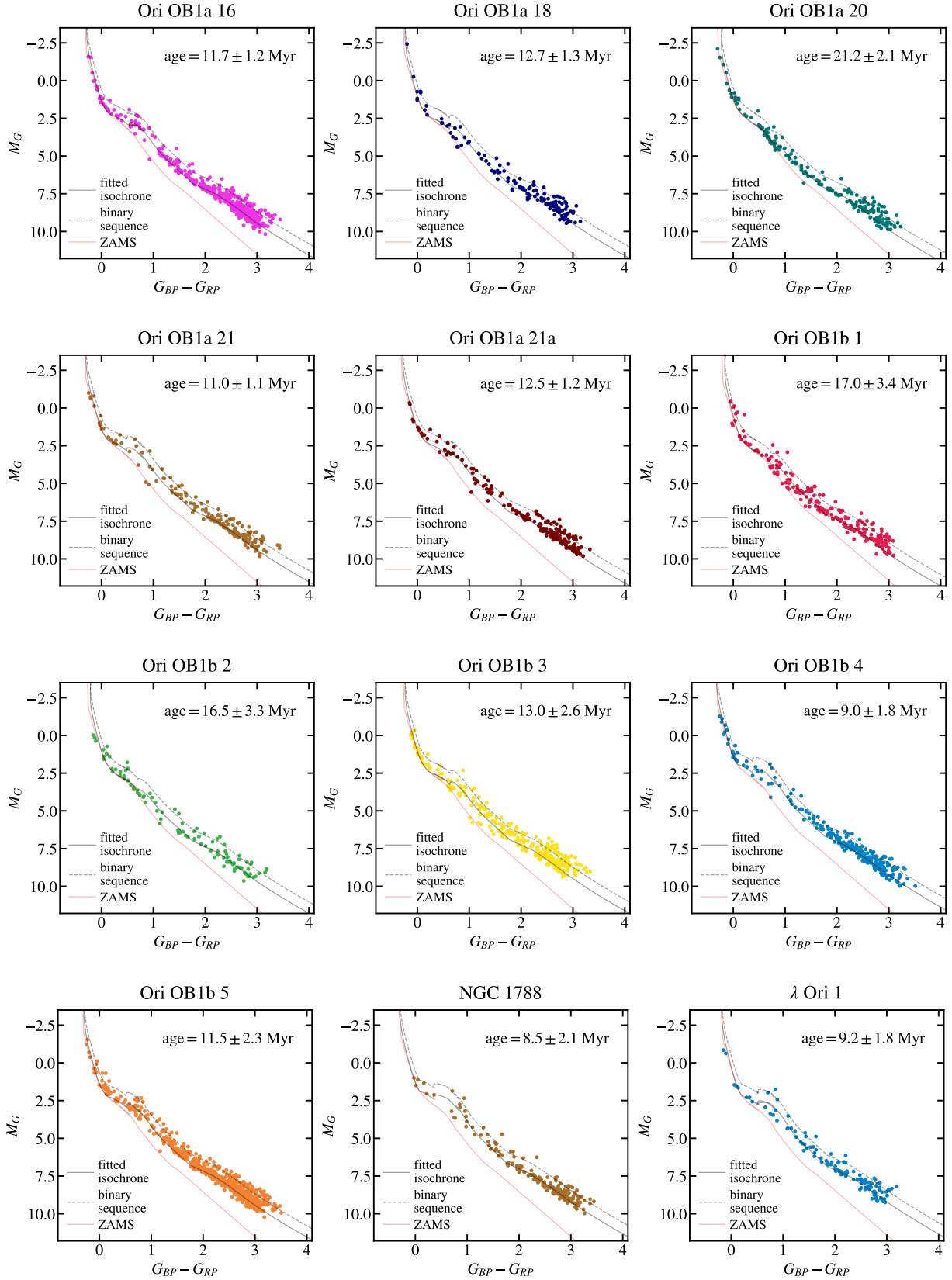


Figure C1. HR diagrams of all 15 clusters used in this work. Age as measured by isochrone fitting is given in each panel. Best fitting isochrone is shown as a solid black line. Dashed line shows its binary sequence. Red line shows the PMS.

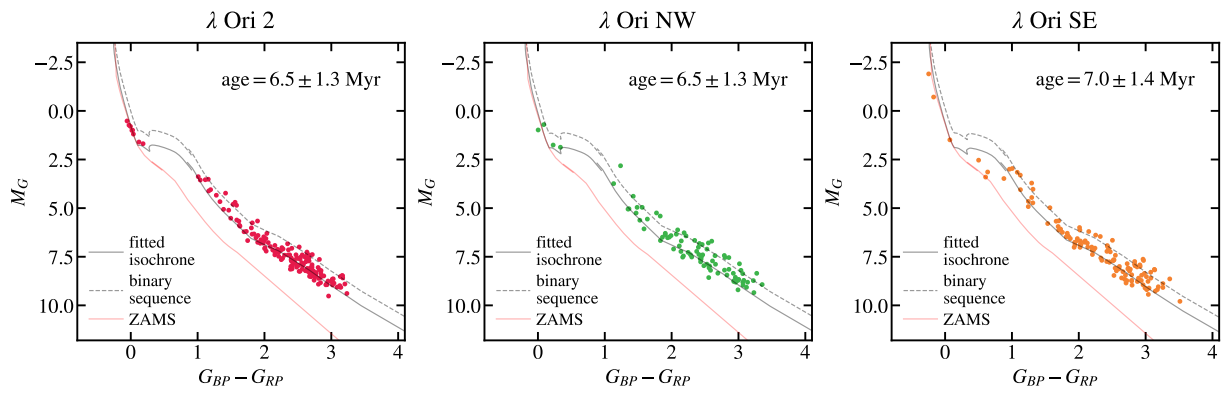


Figure C1. contd.

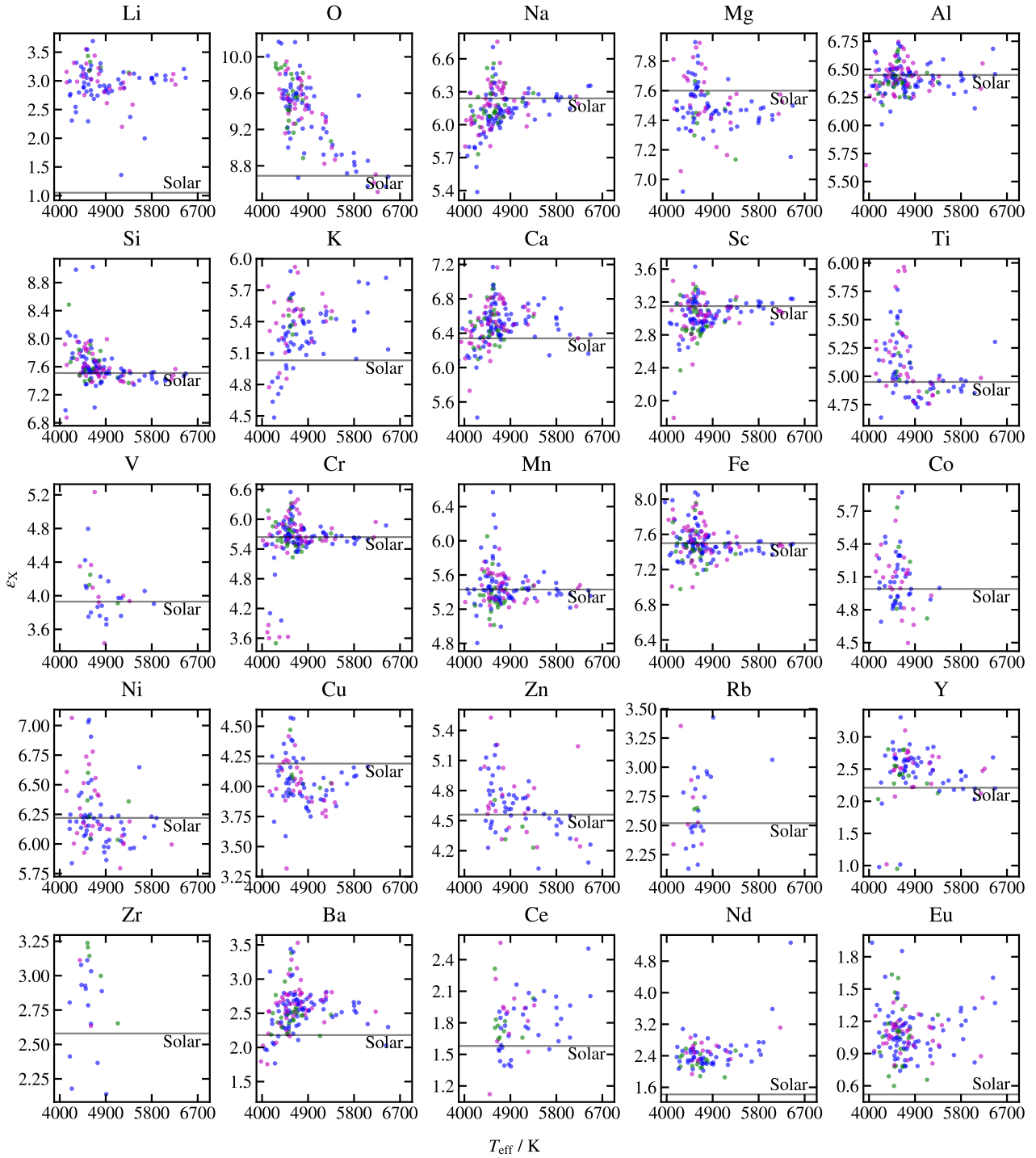


Figure D1. Measured mean abundances of 25 elements given in GALAH DR3 for the same stars as in Figure 11. Stars without measured abundances in GALAH DR3 are missing from this plot.